Coupled mesoscale-LES modelling of air quality in a polluted city using WRF-LES-Chem

Yuting Wang[1], Yong-Feng Ma[2], Domingo Muñoz-Esparza[3], Jianing Dai[4], Cathy W. Y. Li[4], Pablo Lichtig[4], Roy C.W. Tsang[5], Chun-Ho Liu[6], Tao Wang[1], and Guy P. Brasseur[1,4,7]

[1]Department of Civil and Environmental Engineering, the Hong Kong Polytechnic University, Hung Hom, Kowloon, Hong Kong.
[2]Department of Mechanics & Aerospace Engineering, Southern University of Science and Technology, Shenzhen, 518055, China.
[3]Research Applications Laboratory, National Center for Atmospheric Research, Boulder, CO 80301, USA.
[4]Max Planck Institute for Meteorology, 20146 Hamburg, Germany.
[5]Environmental Protection Department, Hong Kong
[6]Department of Mechanical Engineering, The University of Hong Kong, Hong Kong
[7]Atmospheric Chemistry Observation & Modeling Laboratory, National Center for Atmospheric Research, Boulder, CO 80301, USA.

Corresponding author: Yuting Wang (yuting.wang@polyu.edu.hk) and Yong-Feng Ma (mayf3@sustech.edu.cn)

Abstract. To perform realistic high-resolution air quality modeling in a polluted urban area, the Weather Research and Forecasting (WRF) model is used with an embedded large-eddy simulation (LES) module and with online chemistry. As an illustration, a numerical experiment is conducted in the megacity of Hong Kong, which is characterized by multi-type inhomogeneous pollution sources as well as complex topography. The results from the multi-resolution simulations at mesoscale and LES scales are evaluated by comparing them with ozone sounding profiles and surface observations. The comparisons show that both mesoscale and LES simulations reproduce well the mean concentrations of the chemical species and their diurnal variations at the background stations. However, the mesoscale simulations largely underestimate the NO_X concentrations and overestimate O_3 at the roadside stations due to the coarse representation of the traffic emissions. The LES simulations improve the agreement with the measurements near the road traffic, and the LES with the highest spatial resolution (33.3 m) provides the best results. The large-eddy simulations show more detailed structures in the spatial distributions of chemical species than the mesoscale simulations, highlighting the capability of LES to resolve high-resolution photochemical transformations in urban areas. Compared to the mesoscale model results, the LES simulations show similar evolutions in the profiles of the chemical species as a function of the boundary layer development over a diurnal cycle.

1 Introduction

Air pollution represents one of the most important factors affecting human health (WHO, 2013). Human exposure to outdoor air pollution often occurs at the street level in urban canyons, and high-resolution air quality forecasting is therefore required to take appropriate preventive actions and limit air pollution (Barzyk et al., 2015; Sauer and Muñoz-Esparza, 2020). Air quality

at the street level is difficult to simulate, especially if the model resolution is too coarse to properly resolve urban flows. The complexities in the distribution and variation of the chemical species in the urban canopy are due to several factors. First, the

35   heterogeneous emissions, such as vehicle emissions at the street level, are difficult to represent in coarse models. Second, the dispersion of chemical species in turbulent flows cannot be adequately resolved by mesoscale models. Additionally, the nonlinear turbulence-chemistry interactions in the turbulent planetary boundary layer (PBL), which can be important under polluted situations, are ignored in the coarse models (Li et al., 2021; Wang et al., 2021, 2022).

Because air pollution is determined by both local dynamical circulations and long-distance transport, the accurate simulation

40   of the species' distribution requires that mesoscale and microscale processes be coupled. Regional models, which adopt global or coarser regional model output as initial and boundary conditions, are usually applied at the spatial resolution of several kilometers, with the effects of turbulent motions being parameterized through commonly used one-dimensional PBL schemes. Mesoscale models can therefore reproduce regional-scale air pollution, but are not adequate for simulating the distribution of physical and chemical variables at the urban neighborhood scale, which requires that the model resolution be less than 1 km.

45   Moreover, the representation of air pollution near road traffic requires further increasing of the model resolution to be smaller than 40 m (Batterman et al., 2014). In order to explicitly resolve buildings in the models to fully account for the urban effects, the grid spacing should further be increased to at least 10 m (Maronga et al., 2019).

Different downscaling methods are used to represent detailed air pollution distributions in urban or industrial areas. Due to their high computational efficiency, models based on a Gaussian-type redistribution of the wind flow (Forehead and Huynh,

50   2018) are often adopted to represent chemical species in street canyons. However, these types of models do not directly calculate dynamical and thermal processes and ignore therefore turbulence-chemistry interactions. To better predict the nonlinear photochemical reactions in the PBL over complex underlying surfaces, the turbulent eddies need to be explicitly resolved.

There are three main basic approaches can be used to account for the effects of turbulence on the chemical species: the

55   Reynolds-averaged Navier-Stokes (RANS) formulation, the Large-Eddy Simulation (LES) approach, and the Direct Numerical Simulation (DNS) method. Among these models, RANS requires the least computational resources, but can only resolve the mean flows and averages out the turbulent fluctuations, while DNS directly resolves all the scales of the eddies without any approximation or parameterization; however, this approach is computationally expensive. LES, which is an intermediate approach between RANS and DNS, is a more common choice, in which the large eddies that contain most of the turbulent

60   energy and are responsible for most of the momentum transfer and turbulent mixing are explicitly resolved, while the small eddies are parameterized using Sub-Grid Scale (SGS) schemes (Smagorinsky, 1963; Deardorff, 1970).

Computational Fluid Dynamics (CFD) models resolve turbulence using RANS, LES, or DNS to solve engineering problems involving fluid flows. These models are being increasingly often applied to address urban pollution problems, which has become possible with the availability of large computational resources. The advantage of the CFD approach is that it can

65   resolve the urban morphology (e.g., terrain, buildings, streets, and so on), thus explicitly calculate the eddies across the streets and around the buildings. Such models represent the effects of the urban canopy on the dynamics of flows. They also simulate

pollutant retention at street level, typically at a resolution of meters; however, their domain is usually limited to a few kilometers squared (Tominaga and Stathopoulos, 2013; Zhong et al., 2016). Many studies coupled mesoscale models with CFDs to investigate micro-scale processes in realistic applications (Baik et al., 2009; Zheng et al., 2015). However, due to the

70 large gap between scales in mesoscale and CFD formulations, the processes covering intermediate scales are missing. In addition, CFD modules mainly focus on dynamical processes in the flow field, but do not describe other major atmospheric processes related to physics, thermodynamics, radiative transfer, cloud processes, land surface exchanges, etc.

LES formulations on the other hand can also be applied in meteorological models with full physical and chemical processes in a spatial domain that is considerably larger than a common CFD domain. An illustrative example (Khan et al., 2021) of an

75 LES module with atmospheric chemistry linked to regional information is provided by the Parallelized Large-eddy Simulation Model (PALM) for urban applications (PALM-4U) applied to an urban environment. To perform realistic studies, the PALM model uses additional tools (e.g. INIFOR, Maronga et al., 2020; WRF4PALM, Lin et al., 2021) to create initial and boundary meteorological conditions from mesoscale models. Recently, efforts by the atmospheric LES community to model urban effects have focused on exploiting the accelerated computing from GPUs (Muñoz-Esparza et al., 2020, 2021; Sauer and

80 Muñoz-Esparza, 2020), since these fine-scale simulations are otherwise computationally too expensive.

The Weather Research and Forecasting (WRF; https://www2.mmm.ucar.edu/wrf/users/; Skamarock, 2019) model allows multiscale nested simulations of the atmosphere with a full suite of atmospheric dynamics, surface exchanges, radiation, and cloud physics. An LES module was embedded into WRF (WRF-LES), which can be applied in two modes: (1) without external forcing from the mesoscale model or by real-world meteorological data (Moeng et al., 2007; Yamaguchi and Feingold, 2012);

85 or (2) by being coupled with the mesoscale WRF (Nozawa and Tamura, 2012; Muñoz-Esparza et al., 2017). The WRF model can also account for atmospheric chemistry (WRF-Chem; https://ruc.noaa.gov/wrf/wrf-chem/; Grell et al., 2005) and specifically simulate the transport and chemical reactions between various species with different mechanisms. In this work, we use the WRF model framework with the LES mode and online chemistry (WRF-LES-Chem) to perform muti-scale simulations of atmospheric chemical species. The advantage of using WRF-LES-Chem is that all the physical and chemical

90 processes are consistent among the different scales. This allows to analyze the differences induced by turbulent interactions. Previous studies using coupled WRF-LES-Chem investigated passive tracer dispersion in urban environments (Nottrott et al., 2014; Gaudet et al., 2017). Here we use a more comprehensive chemical mechanism in the coupled WRF-LES-Chem model to study the ozone photochemistry in a complex terrain.

The model experiments were conducted for the city of Hong Kong, a highly urbanized area with severe air pollution. The

95 region is characterized by heterogeneous land use with forest over the mountains and dense constructions along the coast. The pollution originates from different sources including road transport, navigation, civil aviation, power plants, industry, hill fires, and other combustion and non-combustion emissions. The complex topography, land surface, and diverse emissions make it difficult to predict the air quality patterns and variability in the city, especially in the dense built-up area. Hong Kong therefore poses challenging questions that can be investigated with a high-resolution model and offers a perfect scenario to evaluate the

100 capability of WRF-LES-Chem to perform high-resolution air pollution predictions.

The purpose of this work is to exploit the WRF framework with embedded LES and chemistry modules to conduct realistic high-resolution air quality simulations in a densely populated urban area. The model setup is presented in Section 2. The description of the observations can be found in Section 3. In Section 4, the performance of the WRF-LES-Chem model is evaluated by comparison to available observations. The influence of spatial resolution on the model results is also presented, including the impact of the resolved turbulence on atmospheric chemistry by comparing it to mesoscale model output with PBL parameterization. Section 5 summarizes the study and provides conclusions.

2 Model setup

2.1 Dynamic settings

The WRF model coupled with chemistry (version 4.0.2) is used in the present study. The coupled mesoscale and LES module within WRF are adopted to represent spatial and temporal scales specifically capturing synoptic to turbulent motions. The model setup consists of seven one-way nested domains, out of which D01-D04 are mesoscale domains and D05-D07 are LES domains (Fig. 1). The horizontal resolutions for the mesoscale domains are 24.3 km, 8.1 km, 2.7 km, and 900 m, respectively from the outer to inner domains, with the number of points in the zonal and meridional directions of 141×141, 141×141, 141×141, and 180×180 in the corresponding domains. The grid spacings in the LES domains are 300 m, 100 m, and 33.3 m, respectively for D05 to D07, and the corresponding grid numbers are 240×240, 396×342, and 243×243. The vertical layers are set to 63 levels for all the domains, with the finest vertical resolution of 12.5 m to 50 m in the lowest 1.3 km (30 layers). For the heights above 1.3 km, the vertical spacing increases gradually towards the model top located at 50 hPa.
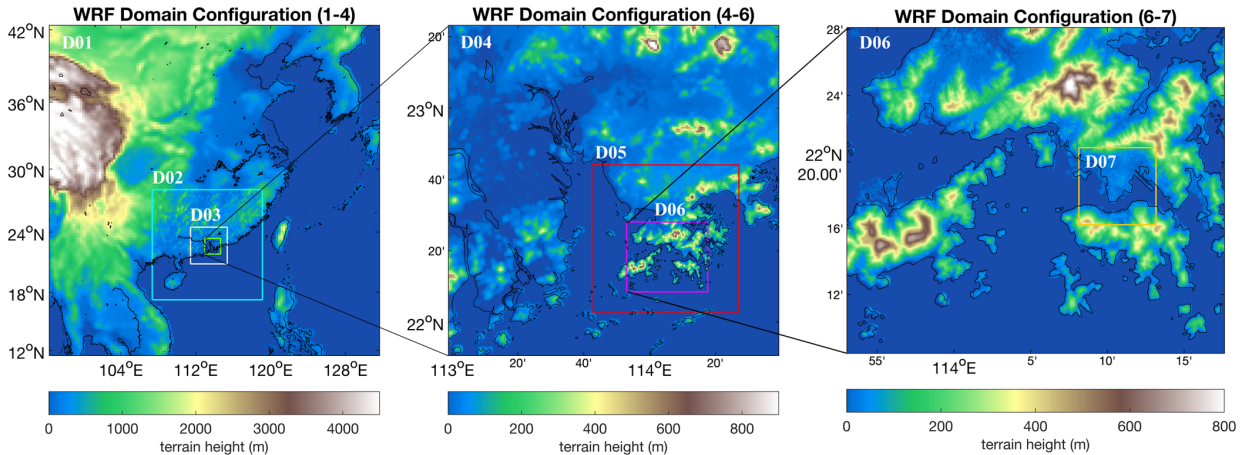
Figure 1. Setup of the seven one-way nested WRF domains and a representation of the topography adopted in the model.

The meteorological initial and boundary conditions are obtained from the Final Operational Global Analysis (FNL) data produced by the National Centers for Environmental Prediction (NCEP) on $1° \times 1°$ grids and 6-hour intervals. The topography data for D01-D05 are from the Global Multi-resolution Terrain Elevation Data (GMTED2010) 30-arc-second dataset

4

developed by the U.S. Geological Survey (USGS) and the National Geospatial-Intelligence Agency (NGA). For the two innermost domains D06 and D07, the terrain heights are adopted from the ALOS world 3D data (Takaku et al., 2014) distributed by OpenTopography (https://opentopography.org; last access: Jun 1, 2020) with a spatial resolution of 30 m. The topography maps after pre-processing are shown for different domains in Fig. 1. The land use data are obtained from the Noah-modified 21-category Moderate Resolution Imaging Spectroradiometer (MODIS) database developed by International Geosphere-Biosphere Programme (IGBP) on 30-arc-second resolution (Friedl et al., 2010).

The Yonsei University (YSU; Hong et al., 2006) PBL scheme is adopted in the mesoscale domains to parameterize the SGS turbulent fluxes within the PBL. The PBL parameterization, however, is turned off in the LES domains, where the large eddies are directly resolved and the effects of the small eddies are expressed by the three-dimensional 1.5-order TKE subgrid closure of Deardorff (Deardorff, 1970; Moeng, 1984). Most of the other main physical parameterizations are identical for both mesoscale and LES domains. They include the RRTM longwave radiation scheme (Mlawer et al., 1997), the Goddard shortwave radiation scheme (Chou, 1994), the Lin microphysics scheme (Lin et al., 1983), the Noah land surface model (Chen and Dudhia, 2001), and the revised MM5 Monin-Obukhov surface layer scheme (Jiménez et al., 2012). For the coarser mesoscale simulations (D01-D03), the Grell-Freitas cumulus scheme (Grell and Freitas, 2014) is used, while it is turned off in the innermost mesoscale domain (D04) and the LES domains. The urban canopy scheme is turned off in both mesoscale and LES domains.

The simulations of the mesoscale WRF and WRF-LES are performed separately. The mesoscale simulations run from 00:00 UTC on July 30, 2018, to 12:00 UTC on August 1, 2018, and the first 45 hours are considered as a spin-up period. This longtime spin-up ensures that the atmosphere is in balance with the new sea surface temperature and soil properties, and that the atmospheric chemistry reaches an equilibrium state. The output from the innermost mesoscale domain D04 with a time interval of 10 min is taken as the initial and boundary conditions for the LES runs. The LES simulations run from 21:00 UTC on July 31, 2018, to 12:00 UTC on August 1, 2018, which corresponds to the Hong Kong local time (LT) of 05:00 to 20:00 on August 1, 2018. To accelerate the generation of the turbulence in the outer LES domain, the cell perturbation method (Muñoz-Esparza et al., 2014, 2015, 2017) is applied to D05. This method employs a novel stochastic approach based on finite amplitude perturbations of the potential temperature field applied within a region near the inflow boundaries of the LES domain. The perturbations accelerate the transition from the mesoscale flow to a fully developed turbulent state. Since the grid space of D05 is 300 m, which is relative coarse for LES, we consider this case to represent an intermediate domain to pass synoptic motions from mesoscale domains (with turbulence generated in D05) to the smaller LES domains. Therefore, the analysis will focus on the innermost mesoscale domain D04 and the fine LES domains D06 and D07. The first hour from the LES simulations is considered as spin-up time. Since the atmosphere reaches an equilibrium after the spin-up time in the mesoscale domains, the one-hour spin-up for LES domains primarily aims to allow the turbulence to fully develop. Usually, turbulence is fully developed within 30 minutes due to the combined effects of terrain, daytime surface heating, and the application of the cell perturbation method (Muñoz-Esparza and Kosović, 2018). The output intervals for LES domains are 5 min for D05, 2 min for D06, and 1 min for D07.

2.2 Chemical settings
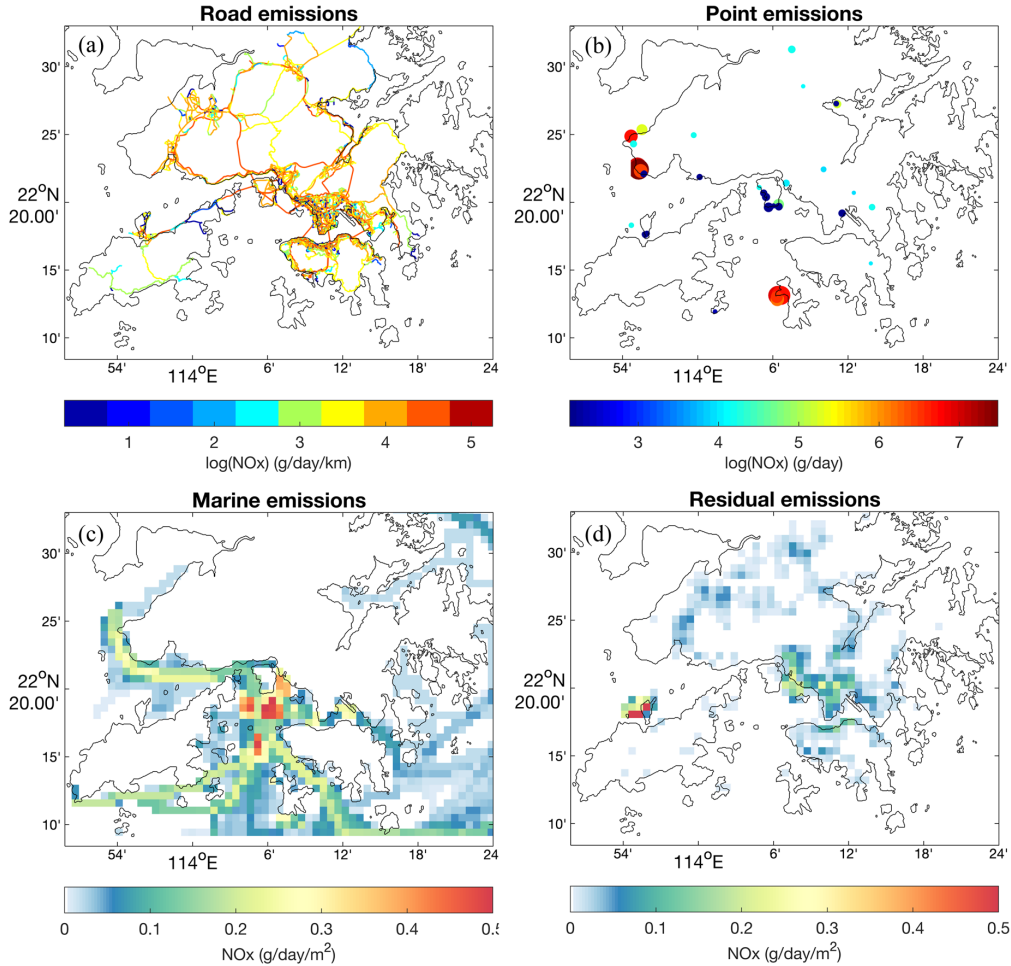
Figure 2. Emission maps of NO_X provided by HKEPD for the Hong Kong region from road (a), point (b), marine (c), and residual (d) sources. The road emissions are shown as line sources for every road with the unit of g day^{-1} km^{-1}. For simplification, all the roads, including those above and below ground, are added in one layer at the surface. The point sources include power plants, industries, crematoriums, and tank farms, with the unit of g day^{-1} per point. The sizes of the points indicate the height of the source. The marine and residual emissions are area sources provided with a 1 km × 1 km resolution with the unit of g day^{-1} m^{-2}.

In the present study, we adopt the Regional Acid Deposition Model, 2nd generation (RADM2; Stockwell, 1990) chemical mechanism with 63 chemical species and 157 reactions. While most chemical species are transported in the model, several fast-reactive species such as the organic peroxy radicals are assumed to follow local photochemical equilibrium conditions. When considering the turbulent flow in the LES simulations with an integration time shorter than the chemical reaction time, the fluctuations in the concentration of these species in the flow, which result in the segregation effect, cannot be ignored. Therefore, the transport of the fast-reactive radicals is turned on in the LES domains. The TUV radiation transfer scheme is

6

170 used for the calculation of the photolysis rates. The initial and boundary conditions for the chemical species are taken from the Community Atmosphere Model with chemistry (CAMChem; Emmons et al., 2020) output (Buchholz et al., 2019).

To cover the entire simulation domains, the anthropogenic emissions adopted in our simulations include the Multi-resolution Emission Inventory for China (MEIC; http://meicmodel.org, last access: 13 May 2022; Zheng et al., 2018) for the year 2017, the MIX emissions for Asia outside of China for the year 2010 (Li et al., 2017), and the international ship emissions from the

175 Emissions Database for Global Atmospheric Research (EDGAR; https://edgar.jrc.ec.europa.eu, last access: 13 May 2022; Johansson et al., 2017) based on the year 2015. We use these emission inventories for the specific year because it is the most updated year that is publicly available. In order to have more detailed emission information in the focused area, we also employ the Pearl River Delta region (PRD) emissions with a resolution of 3 km based on year 2014 (Zheng et al., 2009; Bian et al., 2019). The emission data for Hong Kong are provided by the Hong Kong Environmental Protection Department (EPD) for

180 scientific research purposes, which include road-based vehicle emissions for year 2014, point emissions of power plants, industries, crematoriums, and tank farms for year 2017, marine emissions with a resolution of 1 km for ear 2015, and residual emissions (total emissions subtract the road, marine, and point emissions) on 1 km resolution for year 2015. The emission maps of NO_X from different sources are shown in Fig. 2 as an illustrative example. The Hong Kong emissions are scaled to the simulation year of 2018 according to the annual trend

185 (https://www.epd.gov.hk/epd/english/environmentinhk/air/data/emission_inve.html, last access 13 May 2022). As for the temporal resolution of the emission input data, the gridded emissions are on hourly basis, and the road and point emissions are scaled to the hourly values with the corresponding diurnal profiles (see Fig. S1). The biogenic emissions are calculated with the online Model of Emissions of Gases and Aerosols from Nature (MEGAN; Guenther et al., 2006) embedded in WRF-Chem.

3 Observational data

190 ### 3.1 Surface monitoring network

Hourly-averaged air quality monitoring data are obtained from the Hong Kong EPD's network (https://cd.epic.epd.gov.hk/EPICDI/air/station/?lang=en, last access: 13 May 2022). Among all the stations, there are three roadside stations (Mong Kok, Central, and Causeway Bay) and 13 general stations (relative to roadside stations; see Fig. 3). The general stations can be further categorized as urban, suburban, and rural stations. The information about the stations is

195 listed in Table 1. Because of the limitation of the sizes of the inner domains, the observation stations are not covered by all the domains. The mesoscale domains (D01-D04) and the outer LES domain (D05) cover all the stations. For the smaller LES domains, D06 covers all the stations except of the Tap Mun station, and D07 only covers the roadside stations and three general stations. The instrument heights are below 5 m above ground for the roadside stations, while they are between 10 m and 30 m for the general stations. We use the first layer of the model data to compare between the surface measurements and the model

200 simulations. During the simulation period, no NO_X measurements are available at the Eastern station, and some data are also missing around noon time at the Tsuen Wan and Kwai Chung stations.
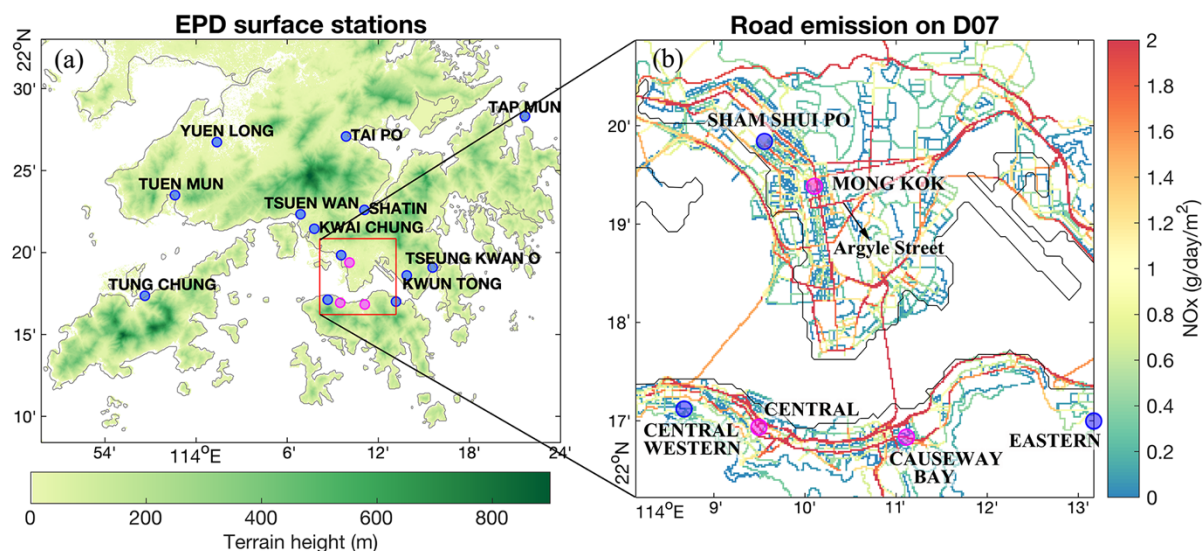
Figure 3. Locations of the surface monitoring stations represented on the map of the Hong Kong topography (a) and the road emissions interpolated to D07 domain grids (b). The blue circles represent the general stations and the magenta circles the roadside stations.

205

Table 1. List of surface stations in Hong Kong EPD's network

Station	Type	Latitude [° N]	Longitude [° E]	Altitude above ground [m]	Covered by domains	Species used
TAP MUN	General-Rural	22.4713	114.3607	11	1-5	NO$_X$, O$_3$
YUEN LONG	General-Suburban	22.4452	114.0227	25	1-6	NO$_X$, O$_3$
TAI PO	General-Suburban	22.4510	114.1646	28	1-6	NO$_X$, O$_3$
TUEN MUN	General-Suburban	22.3912	113.9767	27	1-6	NO$_X$, O$_3$
TUNG CHUNG	General-Suburban	22.2889	113.9437	27.5	1-6	NO$_X$, O$_3$
SHATIN	General-Suburban	22.3763	114.1845	25	1-6	NO$_X$, O$_3$
KWAI CHUNG	General-Urban	22.3571	114.1296	13	1-6	NO$_X$, O$_3$
TSUEN WAN	General-Urban	22.3718	114.1145	17	1-6	NO$_X$, O$_3$
KWUN TONG	General-Urban	22.3096	114.2312	14.7	1-6	NO$_X$, O$_3$
TSEUNG KWAN O	General-Urban	22.3177	114.2596	16	1-6	NO$_X$, O$_3$
SHAM SHUI PO	General-Urban	22.3302	114.1591	17	1-7	NO$_X$, O$_3$
CENTRAL/WESTERN	General-Urban	22.2849	114.1444	16	1-7	NO$_X$, O$_3$
EASTERN	General-Urban	22.2829	114.2194	15	1-7	O$_3$
MONG KOK	Roadside	22.3226	114.1683	3	1-7	NO$_X$, O$_3$
CENTRAL	Roadside	22.2818	114.1581	4.5	1-7	NO$_X$, O$_3$
CAUSEWAY BAY	Roadside	22.2801	114.1851	3	1-7	NO$_X$, O$_3$

3.2 Ozone sounding profile

The ozone sounding measurements at the King's Park station (22.311° N, 114.172° E) in Kowloon peninsula were conducted

210 by Hong Kong Observatory (HKO). We downloaded the measurement data used for model comparison in this study from the

8

World Ozone and Ultraviolet Radiation Data Centre (WOUDC; https://woudc.org/home.php, last access: 13 May 2022). The profile for the simulation period was derived at 05:55 UTC on 1 August 2018, which corresponds to noon time (13:55 LT), when the convective boundary layer is well developed. The trajectory of the sounding is shown in Fig. 4. For the comparison between models and sounding measurements, the vertical profiles are usually taken at the location of the site, because of the coarse resolution of the models. In fact, the sounding balloon drifted over large horizontal distances in response to the background winds during its ascent. In the case adopted in the present study, the balloon drifted about 1.4 km away from its release location before it reached the level of 2 km, and it drifted over a distance of 8.6 km at 10 km altitude. Therefore, as for the high-resolution model simulations in this study, we adopt the nearest model grids along the sounding trajectory for a more precise comparison.
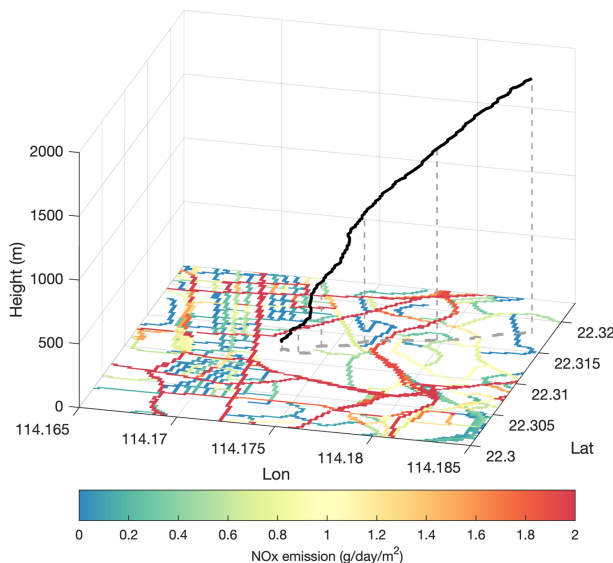
Figure 4. Ozone sounding trajectory in the first 2 km over the road emission map adopted for the innermost domain D07.

4 Results

4.1 General PBL structure

We first evaluate the development of the boundary layer structure in the simulations by comparing model results with sounding profiles at 13:55 LT (Fig. 5). A sharp inversion can be seen in the profiles of the potential temperature and water vapor near the top of the boundary layer, of which this height is usually used to quantify the development of the PBL (Garratt, 1994). For the mesoscale simulations, the PBL height (PBLH) in the model is diagnosed by the YSU PBL scheme. The YSU PBLH for the mesoscale domain (D04, Δ = 900 m) at the nearest grid of the sounding location is 992 m above the surface as shown by the dotted horizontal bar on the D04 profile. In the case of the sounding profiles and the LES model results, the PBLH is determined by applying the bulk Richardson number (Ri_b) method (Hong et al., 2006), which is similar to the approach used in the YSU scheme. The bulk Richardson number is calculated by

9

$$Ri_b = \frac{g[\theta_v(z) - \theta_{vs}]z}{\theta_{vs}[u(z)^2 + v(z)^2]} \tag{1}$$

where θ_v is the virtual potential temperature, θ_{vs} is the virtual potential temperature at the surface, u and v are horizontal wind components, g is gravitational acceleration. The PBLH is defined as the height where Ri_b first exceeds a threshold value of zero (Hong et al., 2006). The PBLH derived from the relation (1) for D04 is 970 m, which is very similar to the value (992 m) simulated by the YSU scheme. The calculated PBLH are 1132 m and 1204 m for the D06 ($\Delta = 100$ m) and the D07 ($\Delta = 33.3$ m) LES domains, respectively, implying that high-resolution enhances the turbulent mixing and hence raises the boundary layer height. The PBLH derived from the observation profile is 1141 m, which is close to the LES simulations but higher than the value derived in the mesoscale domain D04.
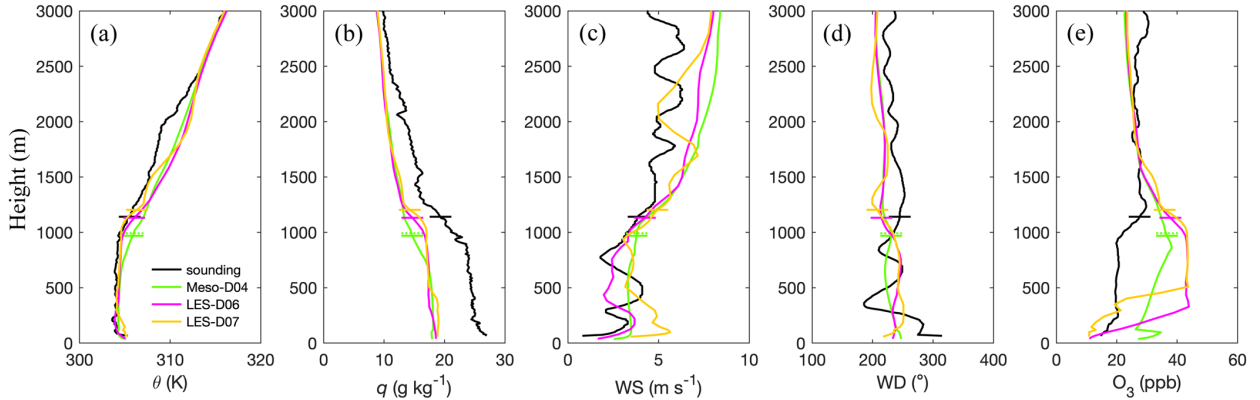
Figure 5. Comparison between ozone sounding measurements and model simulations at 13:55 LT. The variables are the potential temperature (θ; a), the water vapor mixing ratio (q; b), wind speed (WS; c), wind direction (WD; d), and ozone mixing ratio (O_3; e). The black lines represent observations; the green lines the simulations from D04 with resolution of 900 m; the magenta lines the simulations from D06 with resolution of 100 m; and the yellow lines the simulations from D07 with resolution of 33.3 m. The solid horizontal bars indicate the calculated PBLH for each domain, and the dotted horizontal bars show the simulated PBLH from YSU scheme. To further show the profiles in the boundary layer clearer, the same plot but with the altitudes only up to 800 m is shown in Fig. S4.

The potential temperature is generally satisfactorily represented by the simulations for both the mesoscale and the LES domains. However, the mesoscale simulation overestimates the potential temperature near the PBLH, which explains why the calculated PBLH is lower than the observed value. This suggests that the convection in the mesoscale model is relatively weak at this location. All of the simulations underpredict water vapor consistently among all simulation domains, especially at low altitudes; however, this is consistent among all simulation domains. The basic structure of the wind profiles is reasonably well captured by the simulations, but the large fluctuations caused by local turbulence are difficult to replicate by the model in a deterministic manner. Both mesoscale and LES-scale simulations are able to capture the observed southwest wind directions in the lower troposphere, except the near-surface northwest winds. This deviation between simulated and observed winds in the near-surface layer is likely due to the local urban morphology effects, which are not included in the WRF model. Additionally, the surface meteorological observations operated by the Hong Kong Observatory (HKO) are used to validate the model simulations. The map of the used stations is shown in Fig. S2, and the comparison of the averaged diurnal variations is

shown in Fig. S3. Overall, the coupled mesoscale to LES-scale WRF model is found to be capable of reproducing realistic atmospheric conditions for the period of interest.

4.2 Comparison of ozone profile with sounding measurements
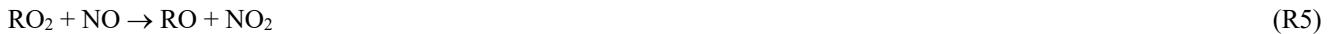
The simulated vertical profiles of ozone are compared to the ozone sounding measurements (Fig. 5). The mesoscale simulation overestimates the ozone concentrations near the surface, probably due to the lack of capability to resolve the road emissions. The emitted NO from traffic sources reacts with O_3 to produce NO_2:

$$NO + O_3 \rightarrow NO_2 + O_2 \tag{R1}$$

Under high pollution conditions, this leads to an increase in NO_2 concentrations and a decrease in the O_3 level. Therefore, the small emission of NO in the coarse resolution model results in a weak titration of ozone and hence an overestimation of the ozone concentration. The LES simulations tend to give a lower level of surface O_3 due to the better representation of the spatial emission distribution and improve the agreement with the measurements, illustrating the advantage of the high-resolution LES. Both mesoscale and LES simulations overestimate the O_3 concentrations within the rest of the PBL above the surface layer, which implies that the O_3 source is overestimated in this region. The formation of O_3 follows the photolysis of NO_2:

$$NO_2 + h\nu \rightarrow NO + O(^3P) \tag{R2}$$

$$O(^3P) + O_2 + M \rightarrow O_3 + M \tag{R3}$$

The combination of reactions (R1) – (R3) results in a null cycle without any net gain/loss of O_3. However, in the presence of volatile organic compounds (VOCs), the RO_X ($RO_X = OH + HO_2 + RO_2$; RO_2 stands for any organic peroxy radical) photochemical cycle continuously supplies HO_2 and RO_2 to oxidize NO into NO_2 without consuming ozone. This mechanism limits the production of O_3 in the troposphere (Wang et al., 2017):

$$OH + RH + O_2 \rightarrow RO_2 + H_2O \tag{R4}$$

$$RO_2 + NO \rightarrow RO + NO_2 \tag{R5}$$

$$RO + O_2 \rightarrow HO_2 + RCO \tag{R6}$$

$$HO_2 + NO \rightarrow OH + NO_2 \tag{R7}$$

where RH represents any non-methane hydrocarbon, and RCO represents carbonyls.

To identify the possible reasons for the disagreement between simulations and observations, the vertical cross sections of the O_3 mixing ratios along the sounding trajectory for the three domains (D04, D06, and D07) are shown in Fig. 6. This graph shows that the O_3 concentrations derived by the mesoscale model are too high within the entire boundary layer depth. In the coupled LES simulations, lower O_3 concentrations can be seen near the surface, which agrees with the measurements. The low O_3 air masses from the surface can reach approximately 80% of the PBL height, indicating a strong vertical mixing. In addition, the air parcels with low O_3 values are clearly transported to higher altitudes by the updrafts produced by the stronger turbulent mixing occurring in the high-resolution LES domain D07. On the other hand, the downdrafts transport the high O_3 air parcels to the lower altitudes (see Fig. 6c). In addition to the low O_3 near the surface, high O_3 air masses can be found in the west of

11

290   the domain, resulting in an overestimation of O_3 between 400 m and 1000 m. The cross sections of OH, HO_2, and RO_2 are also depicted in Fig. 6 (bottom row), which shows high concentrations of OH, HO_2, and RO_2 along with the high O_3 concentrations. As discussed above, the RO_X cycle (R4) – (R7) converts NO to NO_2, and tends to produce O_3 under such conditions. This results in high O_3 in the western part of the domain and in the upper boundary layer. The comparison between the models and the observations indicates that the O_3 distribution in the LES simulations is offset relative to the measurements – the modeled

295   O_3 is shifted to the downwind direction. Fig. 5c shows that the model generally overestimates the horizontal wind speed in the boundary layer, and therefore displaces the air masses with low O_3 too rapidly to the east of the sounding trajectory, which probably explains the overestimation of O_3 between 400 m and 1000 m.
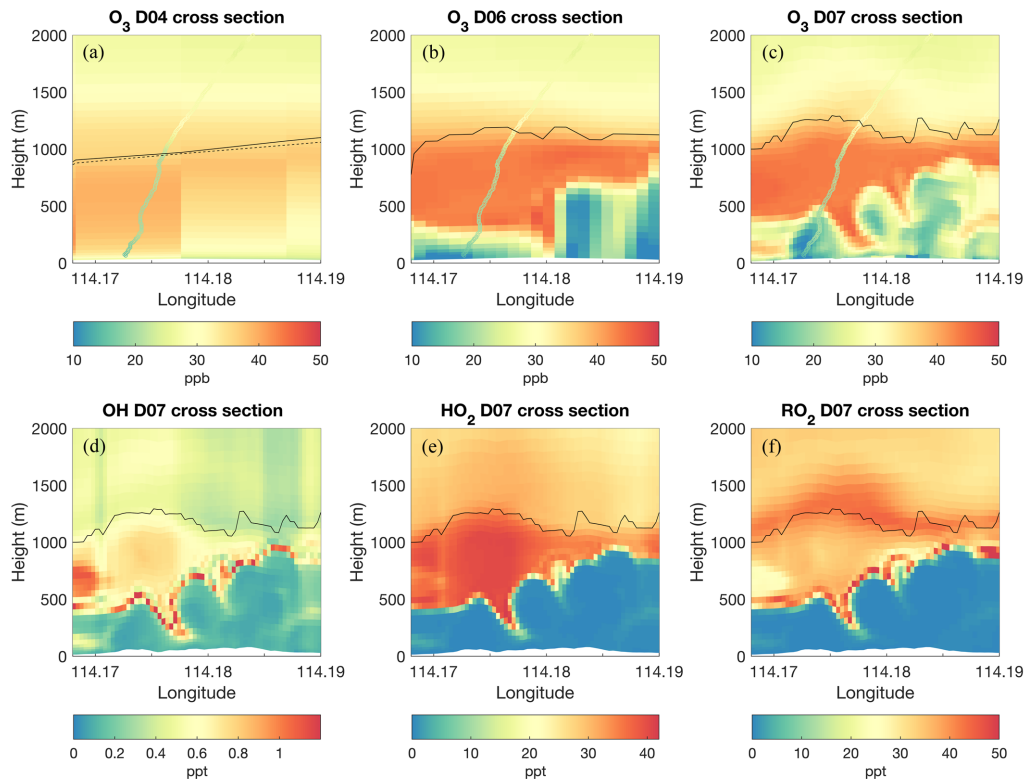

300   **Figure 6.** Top: O_3 mixing ratio (ppbv) cross sections along the balloon sounding trajectory for the D04 (a), D06 (b), and D07 (c) domains. Thick colored lines represent the ozone sounding measurements along the trajectories at 13:55 LT. The black solid lines are PBLH calculated using the bulk Richardson number method, and the black dash line is the PBLH from the model output for the mesoscale domain, which is simulated in the YSU PBL scheme. Bottom: Cross sections along sounding trajectory for D07 of the OH (d), HO_2 (e), and RO_2 (f; sum of the organic peroxy radicals in RADM2 chemical mechanism) mixing rations (pptv).

305   **4.3 Comparison of pollutants with surface observations**

12
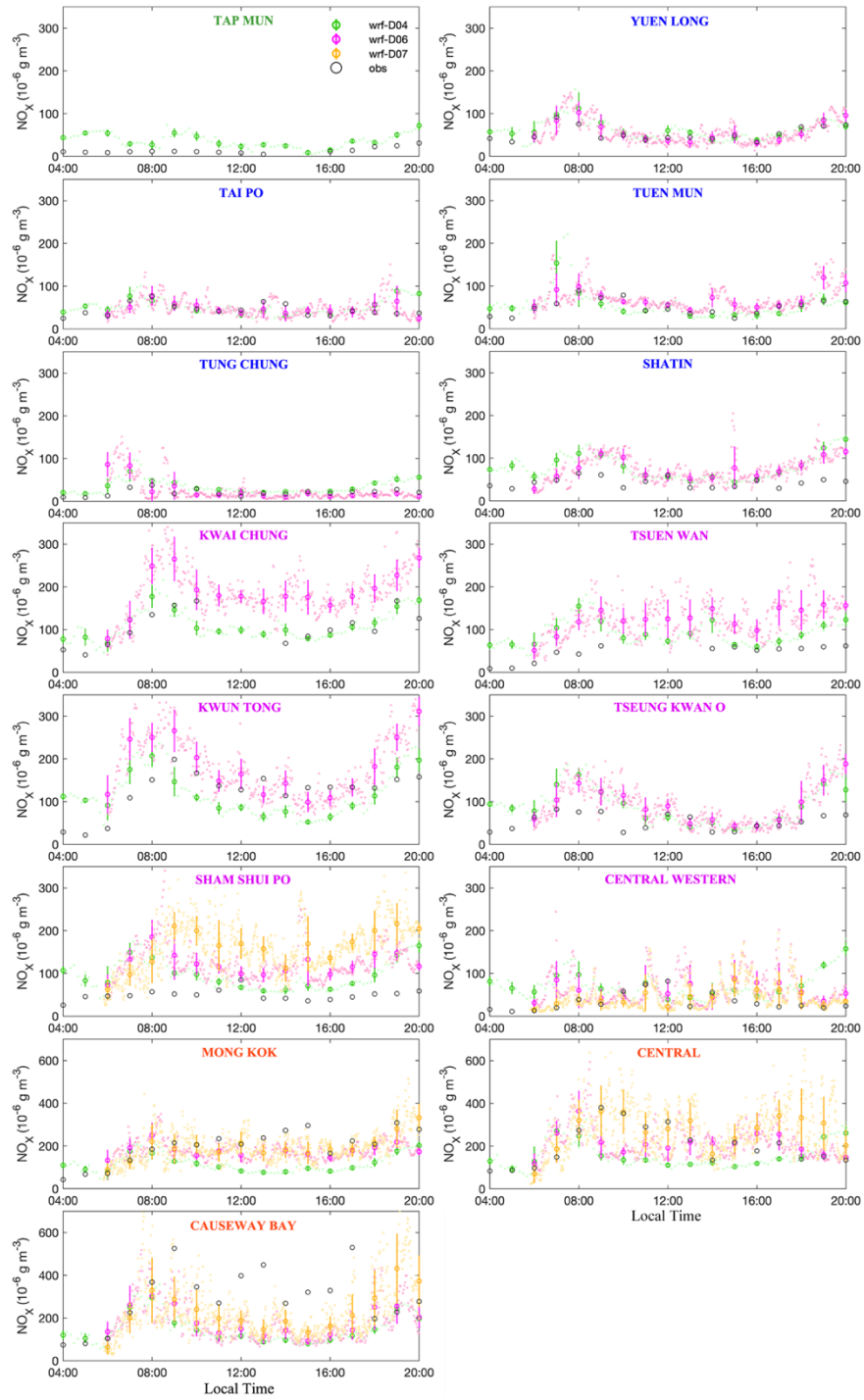
Figure 7. Comparison between NO_X surface measurements and model simulations. Black circles are hourly observations; small dots with different colors (green: D04; magenta: D06; magenta: D07) represent the simulations at output intervals. Dots with error bars refer to the hourly averages with standard deviations. Note that the y-axis is different for the general and roadside stations. The station names are marked with different colors to represent the station types: green – rural, blue – suburban, magenta – urban, red – roadside.

310

13
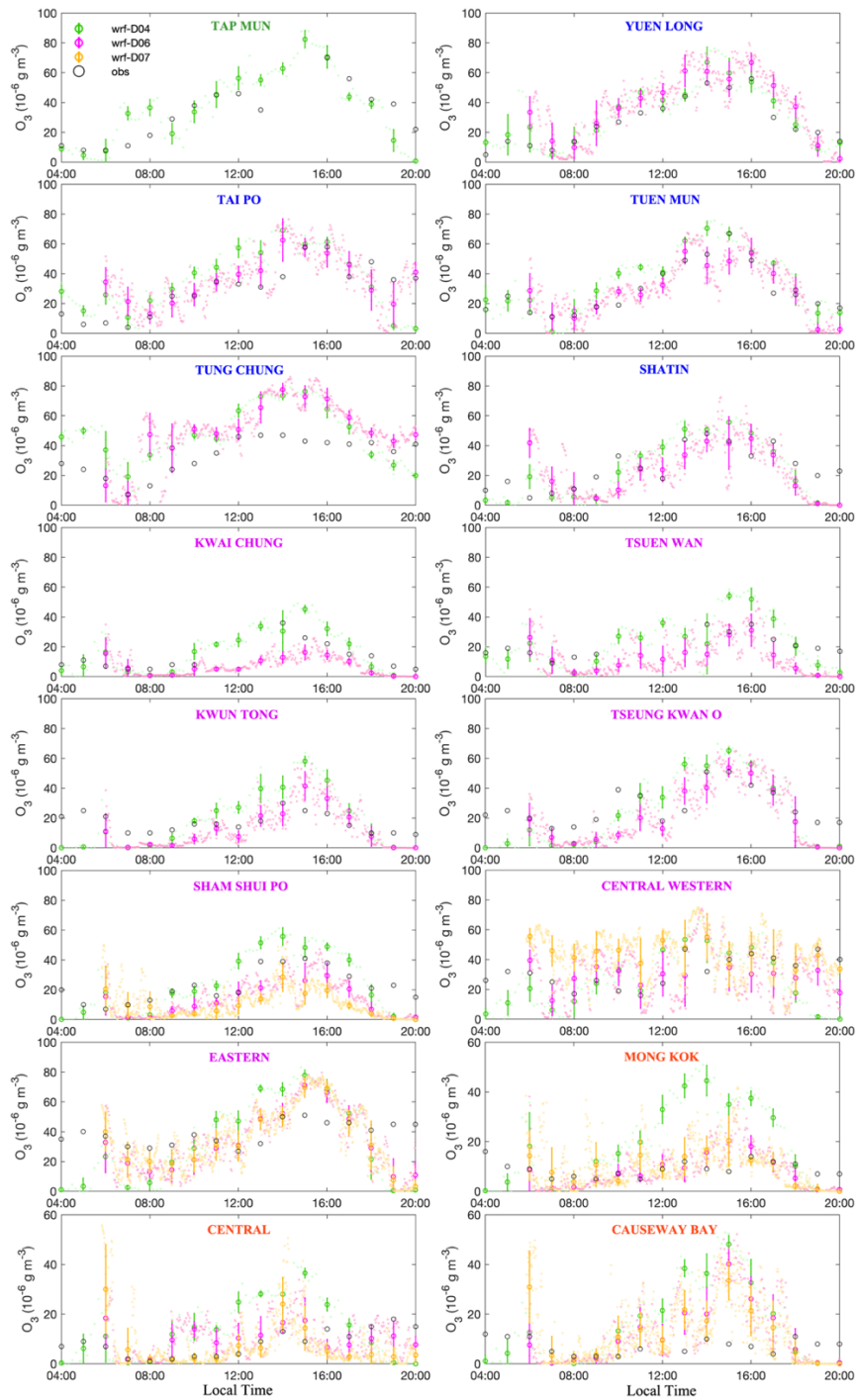
Figure 8. Comparison between O3 surface measurements and model simulations. Black circles are hourly observations; small dots with different colors (green: D04; magenta: D06; magenta: D07) represent the simulations at output intervals. Dots with error bars refer to the hourly averages with standard deviations. Note that the y-axis is different for the general and roadside stations. The station names are marked with different colors to represent the station types: green – rural, blue – suburban, magenta – urban, red – roadside.

14

Figure 7 shows a comparison between simulated NO_X concentrations and surface measurements. We focus here on the model results from the innermost mesoscale domain (D04, 900 m, green dots), the middle LES domain (D06, 100 m, magenta dots), and the innermost LES domain (D07, 33.3 m, yellow dots). At most general stations, the mesoscale simulation of D04 captures well the mean NO_X concentrations and the diurnal variations. The best agreement is found at the stations located in the northern and western rural and suburban areas of Hong Kong, i.e., stations that are far away from the city center including Tap Mun, Yuen Long, Tai Po, Tuen Mun, Tung Chung, and Shatin. The mean NO_X concentrations at these suburban stations are lower than 100 μg m^{-3}. This indicates that the regional models are good at predicting the background levels of the pollutants over a relatively large area. For the urban general stations closer to the emission sources, the simulated NO_X concentrations in the D04 case are higher than the measured values except at the Kwun Tong station. The overestimation of NO_X mainly occurs during the rush hours (7:00-9:00 and 18:00-20:00 LT), implying that the road emissions are overestimated at these locations. As for the roadside stations, as expected, the NO_X values are underestimated in the mesoscale simulation due to the poor representation (too coarse resolution) of the road emissions. The mean biases (MB) and root mean square errors (RMSE) of the simulated against the measured NO_X concentrations are listed in Table 2. The smallest MBs are found at the suburban stations, most of which are below 15 μg m^{-3}. The RMSEs at these stations are between 15 μg m^{-3} and 45 μg m^{-3}. At the urban general stations, the only negative MB is found at the Kwun Tong station, where the mesoscale D04 simulation underestimates the observed NO_X. The MBs at the other urban general stations are all positive, ranging between 30 μg m^{-3} and 50 μg m^{-3}. The RMSEs at the urban general stations are 30 – 60 μg m^{-3}. The MBs and RMSEs for the roadside stations are much higher than those of the general stations. The MBs are all negative at the roadside stations with values of -97.006 μg m^{-3} at Mong Kok, -54.373 μg m^{-3} at Central, and -171.499 μg m^{-3} at the Causeway Bay stations, respectively. The RMSEs range from 117.431 μg m^{-3} to 219.693 μg m^{-3} for the roadside stations.

The 100-m LES (D06) simulation results in mean concentrations and diurnal variations of NO_X that are similar to those from the mesoscale model at the suburban stations, but with larger variances resulting from the explicitly resolved eddies. Some improvements can be seen during evening hours at Tai Po and Tung Chung. The calculated MBs and RMSEs show improvement in the D06 LES simulation at most of the suburban stations when compared to the mesoscale simulation. For example, at the Tai Po station, the MB decreases from 5.574 μg m^{-3} in the D04 simulation to 1.196 μg m^{-3} in the D06 simulation, and the RMSE decreases from 21.846 μg m^{-3} to 13.667 μg m^{-3}. The variances of the simulated NO_X concentrations from D06 are larger at the urban stations closer to the city center, indicating the complexity of the mixing and dispersion of pollutants in the turbulent flows over heterogenous urban surfaces even without the explicit representation of buildings. The agreement between the NO_X concentrations simulated by the 100-m LES and by the measurements is improved at the Central Western urban stations with smaller MB and RMSE, and is worsened at the other urban general stations (e.g., the 100-m LES overestimates the NO_X concentrations at Tsuen Wan, Kwai Chung, Kwun Tong, and Sham Shui Po). In other words, the high-resolution model does not necessarily provide better predictions of the chemical species at the general stations. One possible explanation is that the emission inventories (or their spatial and temporal resolution) are not sufficiently accurate and resolved

15

in time. For instance, the road emissions are based on annual mean traffic flows and their mean diurnal profile, which do not capture the real-time variations. In addition, the road emissions on the overpass are added to the surface layer and thus result in higher NO_X in the simulations at the surface. Also, while higher resolution than standard mesoscale predictions, the LES domains used here do not allow explicit resolution of buildings, which is expected to have a considerable impact in capturing
355 local effects within the urban canopy. As for the roadside stations, the improvements of the 100-m LES simulation are clearer. The D06 simulation provides larger NO_X values than the D04 simulation and agrees more closely with the measurements. This can be seen from the decreased negative biases: MB decreases by about 60 μg m^{-3}, 50 μg m^{-3}, and 30 μg m^{-3}, at Mong Kok, Central, and Causeway Bay, respectively. The RMSEs are also reduced at the three roadside stations. However, there are still disagreements between the D06 simulations and the measurements, for example, the case at Causeway Bay and, between 9:00
360 – 12:00 LT, at the Central station.

Table 2. Statistical parameters to evaluate the modeled NO_X against surface measurements in Hong Kong EPD's network. Both mean bias (MB) and root mean square error (RMSE) are with the unit of μg m^{-3}.

Station	MB (μg m^{-3})			RMSE (μg m^{-3})		
	D04	D06	D07	D04	D06	D07
General-rural						
TAP MUN	24.368	-	-	27.492	-	-
General-suburban						
YUEN LONG	8.271	2.538	-	15.454	13.744	-
TAI PO	5.574	1.196	-	21.846	13.667	-
TUEN MUN	1.118	17.397	-	27.455	24.888	-
TUNG CHUNG	14.370	3.712	-	18.724	24.902	-
SHATIN	34.596	30.122	-	43.717	39.145	-
General-urban						
KWAI CHUNG	4.913	76.343	-	29.672	85.620	-
TSUEN WAN	46.593	72.477	-	55.042	76.611	-
KWUN TONG	-19.761	46.779	-	55.451	73.987	-
TSEUNG KWAN O	31.533	37.823	-	44.669	52.764	-
SHAM SHUI PO	45.230	70.713	109.138	56.432	76.080	117.104
CENTRAL/WESTERN	36.116	23.551	6.627	55.847	36.254	27.552
EASTERN	-	-	-	-	-	-
Roadside						
MONG KOK	-97.006	-38.703	-20.663	117.431	70.419	52.698
CENTRAL	-54.373	-4.965	52.005	126.333	88.712	85.511
CAUSEWAY BAY	-171.499	-139.228	-92.759	219.693	194.115	171.747

365 When the LES grid size is decreased to 33.3 m (D07), the agreement between the simulation and the observations is further improved at the roadside stations. Large improvements can be seen at the Central station in the morning; however, the agreement is worse in the evening. This results in a larger mean bias at the Central station compared to the D06 simulation. The MB at Mong Kok decreases from -38.703 μg m^{-3} in the D06 simulation to -20.663 μg m^{-3} in the D07 simulation, and it reduces from -139.228 μg m^{-3} to -92.759 μg m^{-3} at the Causeway Bay station. For the two urban general stations covered by

370 the D07 domain (note that the Eastern station is covered by D07 but has no NO_X data for the simulation day), the D07 simulation improves the agreement with the measurements at Central Western, with the corresponding MB reduces from 23.551 μg m^{-3} to 6.627 μg m^{-3} and the RMSE decreases from 36.254 μg m^{-3} to 27.552 μg m^{-3}. However, Both MB and RMSE increase at the Sham Shui Po station. The comparison between simulations and observations indicates that increasing the model resolution does not necessarily lead to an improvement over the background air quality simulation, although it can

375 provide a better representation of the air pollution structure over complex land surfaces and near the emission sources.

Next, we compare the simulated ozone concentrations against the observations (refer to Fig. 8), and the statistical skill metrics are listed in Table 3. The interpretation of ozone simulations is more complex because, as opposed to the case of a primary pollutant with a short lifetime like NO_X, which is largely controlled by surface emissions, O_3 is also affected by chemical transformations, dynamic transport, and turbulent mixing. As seen from most of the stations in Fig. 8, the diurnal

380 evolution of the surface O_3 is characterized by low values in the morning and evening, and by high values during daytime with a concentration peak occurring around 14:00 LT, when the photochemical production is largest. The lower O_3 concentrations at the roadside stations compared to those at the general stations are of characteristic of an environment that is NO_X saturated and hence VOC limited. Overall, the mesoscale simulation from D04 matches the observations well at the general stations, suggesting that the representation of the physical and chemical processes in the model is sufficiently realistic. The D04

385 simulation slightly overestimates the O_3 concentrations at most general stations during daytime, but underestimates O_3 in the morning and evening, which is partly attributed to the NO_X overestimation during the rush hour, resulting in the overestimated titration of ozone by NO. The positive MBs at the general stations mostly range from 0.6 μg m^{-3} to 6.6 μg m^{-3} except at the Tung Chung station near the airport in the west of Hong Kong where it reaches 12.970 μg m^{-3}. The negative MBs are in the range between -0.331 μg m^{-3} and -4.463 μg m^{-3}, and mostly occur at the stations in the east of Hong Kong, implying that the

390 model underestimates the O_3 concentration in that region, possibly due to the strong transport of NO_X towards the east by the westerly winds as discussed in Section 4.2. The RMSEs at the general stations are estimated to be between 8.416 μg m^{-3} and 25.257 μg m^{-3}, and the largest value is found at the Eastern station. The O_3 concentrations are overestimated by the mesoscale simulation at the roadside stations as a consequence of the low NO_X traffic emissions in the coarse model. The MBs are 11.671 μg m^{-3} at Mong Kok, 6.208 μg m^{-3} at Central, and 9.830 μg m^{-3} at Causeway Bay, and the corresponding RMSEs are 18.079

395 μg m^{-3}, 13.792 μg m^{-3}, and 18.551 μg m^{-3}, respectively.

When the LES simulation is performed at a 100-m resolution (D06), the O_3 concentrations are reduced at most of the general stations except at the Yuen Long, Tung Chung, and Central/Western stations. Since the mesoscale simulation overestimates the observed O_3 concentrations, this reduction in the O_3 concentration slightly improves the agreement with measurements. The LES also reduces the ozone discrepancies in the evening at the Tai Po, Tung Chung, and Central Western stations.

400 However, the calculated MBs and RMSEs do not show consistent improvement. As for the roadside stations, where a lower level of O_3 concentration is often observed, the simulated O_3 concentrations reproduce the observation better especially at Mong Kok. With the D06 simulation, the agreement at the Central station is also improved, however, with some discrepancies during the morning rush hour. The improvement at Causeway Bay is relatively limited. Both MBs and RMSEs decreased

17

compared to the D04 simulation. The MB is reduced from 11.671 μg m^{-3} to -0.254 μg m^{-3} at Mong Kok, and from 6.208 μg m^{-3} to 1.800 μg m^{-3} at the Central station; the change ranges from 9.830 μg m^{-3} to 5.371 μg m^{-3} at Causeway Bay. The reductions of RMSEs are approximately 13 μg m^{-3}, 7 μg m^{-3}, and 6 μg m^{-3}, for Mong Kok, Central, and Causeway Bay, respectively.

Table 3. Statistical parameters to evaluate the modeled O$_3$ against surface measurements in Hong Kong EPD's network. Both mean bias (MB) and root mean square error (RMSE) are with the unit of μg m^{-3}.

Station	MB (μg m^{-3})			RMSE (μg m^{-3})		
	D04	D06	D07	D04	D06	D07
General-rural						
TAP MUN	-0.331	-	-	14.271	-	-
General-suburban						
YUEN LONG	4.054	7.589	-	8.416	12.304	-
TAI PO	5.110	3.777	-	19.036	13.099	-
TUEN MUN	6.584	-1.392	-	11.322	10.105	-
TUNG CHUNG	12.970	15.428	-	19.392	19.368	-
SHATIN	-0.832	-3.868	-	13.134	15.578	-
General-urban						
KWAI CHUNG	1.663	-6.121	-	8.556	9.410	-
TSUEN WAN	0.616	-8.730	-	12.635	12.517	-
KWUN TONG	4.562	-3.340	-	14.191	8.822	-
TSEUNG KWAN O	-1.323	-7.101	-	14.319	12.853	-
SHAM SHUI PO	2.238	-10.183	-13.115	12.184	12.450	16.375
CENTRAL/WESTERN	-4.463	-1.763	11.644	19.555	13.232	17.681
EASTERN	-3.195	-5.646	-4.958	25.257	17.593	18.279
Roadside						
MONG KOK	11.671	-0.254	1.127	18.079	4.979	6.054
CENTRAL	6.208	1.800	-0.809	13.792	6.626	9.488
CAUSEWAY BAY	9.830	5.371	6.129	18.551	12.674	11.929

In the case of ozone, the high-resolution LES simulation (D07) does not provide improved results at the three general stations and even slightly degrades the model performance relative to the D06 simulation. The MBs from the D07 simulation at Sham Shui Po and Central/Western are larger than those from D06, and the MB at the Eastern station decreases slightly from -5.646 μg m^{-3} for D06 to -4.958 μg m^{-3} for D07. The RMSEs increase modestly at all three general stations. However, as shown in Fig. 8, some improvements can be noticed at the roadside stations. For instance, in the D07 simulation the O$_3$ concentrations are reduced during the morning hours at the Central station, showing a better match with the observation. Although the hourly mean values of O$_3$ from D07 are still too high in the afternoon at Causeway Bay, the observed values are in the range of the variability produced by the high-frequency model output. The MB decreases from 1.800 μg m^{-3} to -0.809 μg m^{-3} at the Central station, while the MBs slightly increase at Mong Kok and Causeway Bay. The presented comparison with surface measurements highlights the existence of larger fluctuations in the pollutant concentrations, which the high-resolution LES model is able to capture in response to more complex turbulent flows in the urban area. These fluctuations may bring the

concentrations of the chemical species closer to the range of measurements, without substantially modifying the average values derived from the statistical analysis of the LES output.

4.4 Spatial distribution of the pollutants

Having validated the model with observations, we now analyze the representation of the spatial distribution of pollutants at different model resolutions. The horizontal distributions of NO, NO_2, and O_3 near the surface for three different model resolutions are shown in Fig. 9 and Fig. 10, at 6:00 LT (morning) and 13:00 LT (noon), respectively. These two times are selected to represent different boundary layer conditions and traffic emissions. To better characterize the differences between model resolutions, we examine our results only in the subregion of D07, which is located in the city center of Hong Kong and is subject to strong traffic pollution. This region corresponds to the area covered by D07, but with the south and west edges of the domain removed to limit the influence from the mountains and the ocean.

At 6:00 LT, around the sunrise, the NO concentrations are very low, because NO has been consumed by the O_3 during the night and the photolysis of NO_2 is still weak at 6:00 LT. Additionally, the rush hour usually starts at 8:00 LT, so that the direct emission of NO from the road traffic is weak. In the case of the mesoscale domain, the horizontal distribution of chemical species in D04 appears on the figure as mosaic tiles with little spatial variations due to its coarse model resolution (see the first row in Fig. 9). In the case of the LES domains D06 and D07, the road NO emissions can be seen on the maps; in particular, the 33.3-m LES produces a distribution of NO in which the presence of the streets is clearly visible. Due to the morning transition, the dispersion of the NO is very weak in the early morning. Contrary to the situation with NO, NO_2 is not directly emitted at the surface, but it is rapidly produced by the conversion from NO. Therefore, the distribution of NO_2 is not as concentrated along the traffic routes as that of NO, but is more influenced by the air flows. In the early morning, the boundary layer transits from stable to unstable conditions, and the combined effect of shear and surface heating plays an increasingly important role in turbulence generation (Beare, 2008), causing the flow to evolve into horizontal rolls oriented along the mean wind direction (southwesterly in this case, see Fig. 9h, l). As a result, a clear strip-like structure associated with convective rolls is visible in the NO_2 distribution patterns, especially in the LES model with 33.3-m resolution (see Fig. 9j). Similarly, the O_3 distribution is influenced by the air flow, showing an opposite feature compared to the pattern of NO_2 since surface O_3 is strongly titrated by NO. To some extent, the spatial distribution of NO_2 and O_3 can be explained by the pattern of vertical wind speed (Fig. 9h, l). The narrow strip-like updrafts in the southwest direction transport the high surface NO upwards to consume O_3, resulting in narrow regions of high (low) concentrations of NO_2 (O_3) above the near-surface layer.

At 13:00 LT, the NO concentrations are higher than those at 6:00 LT, due to increased traffic emissions during daytime (see Fig. 10). Moreover, the NO emitted on the streets exhibits an obvious diffusion phenomenon in the LES domains at noontime in response to the enhanced turbulent mixing and the higher-resolution emission distribution applied to the model. The changes with time in NO_2 and O_3 concentrations at different locations and with different model resolutions are partially due to the complex photochemical reactions. After sunrise, convective instability in the PBL gradually increases, which causes the stronger turbulent mixing and the structure of turbulent flows changes from roll-like to cell-like patterns, yet is disturbed by

19

the presence of terrain and land cover heterogeneities. This can be seen from the cellular structures of the vertical wind speeds, and specifically from the comparable intensity of stronger narrow updrafts and wide downdrafts in the more convective boundary layer (see Fig. 10l). Such stronger mixing results in clearly cellular structures in the NO_2 and O_3 concentration distribution at noontime in the LES D07 domain, but not in the mesoscale domain D04 and in the coarse resolution LES D06 domain.

460
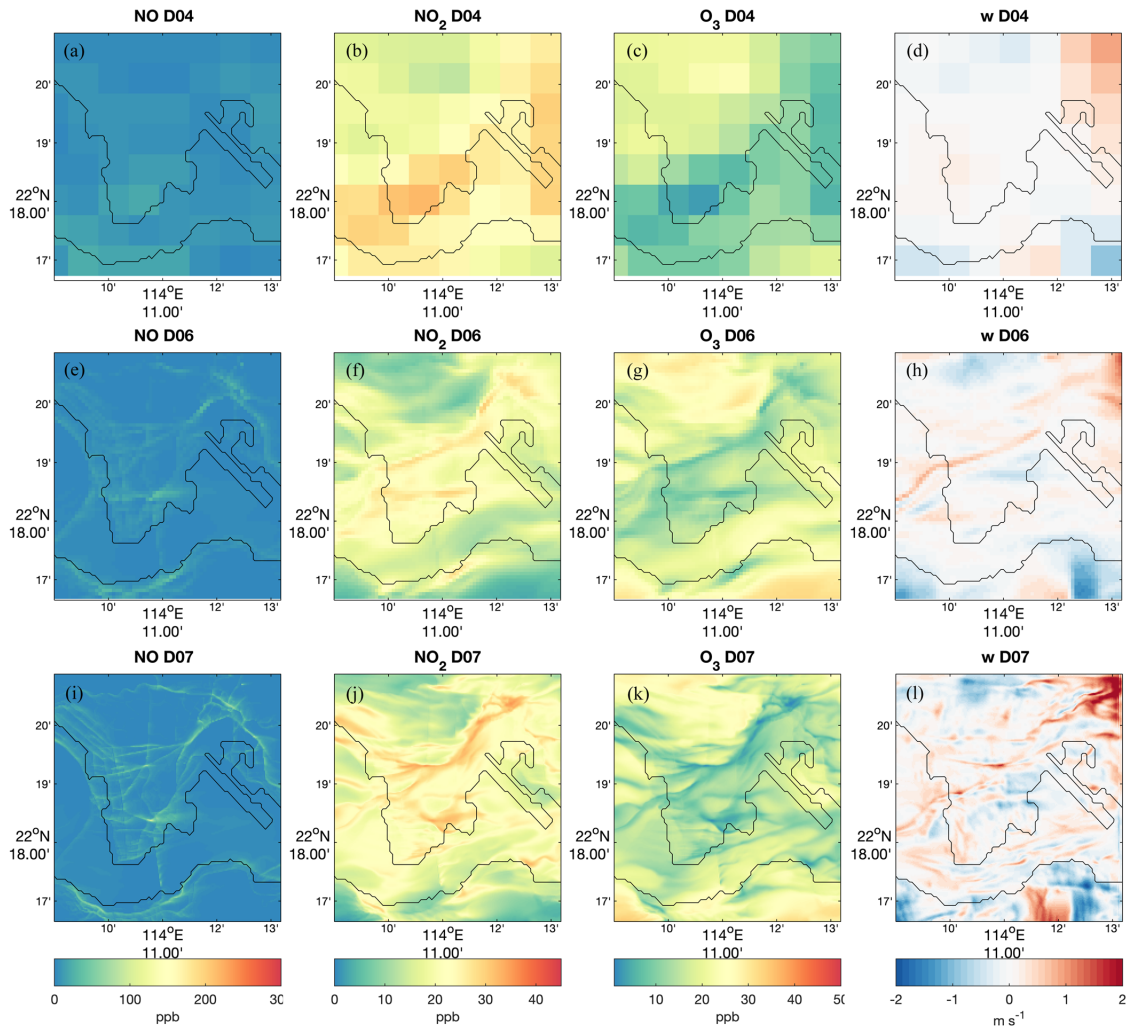
Figure 9. Horizontal distribution of simulated NO (first column), NO_2 (second column), and O_3 (third column) near surface at 6:00 LT for the D04 (first row), the D06 (second row), and the D07 (third row) cases. The fourth column provides the horizontal distribution of vertical wind (w) at approximately 100 m above ground.
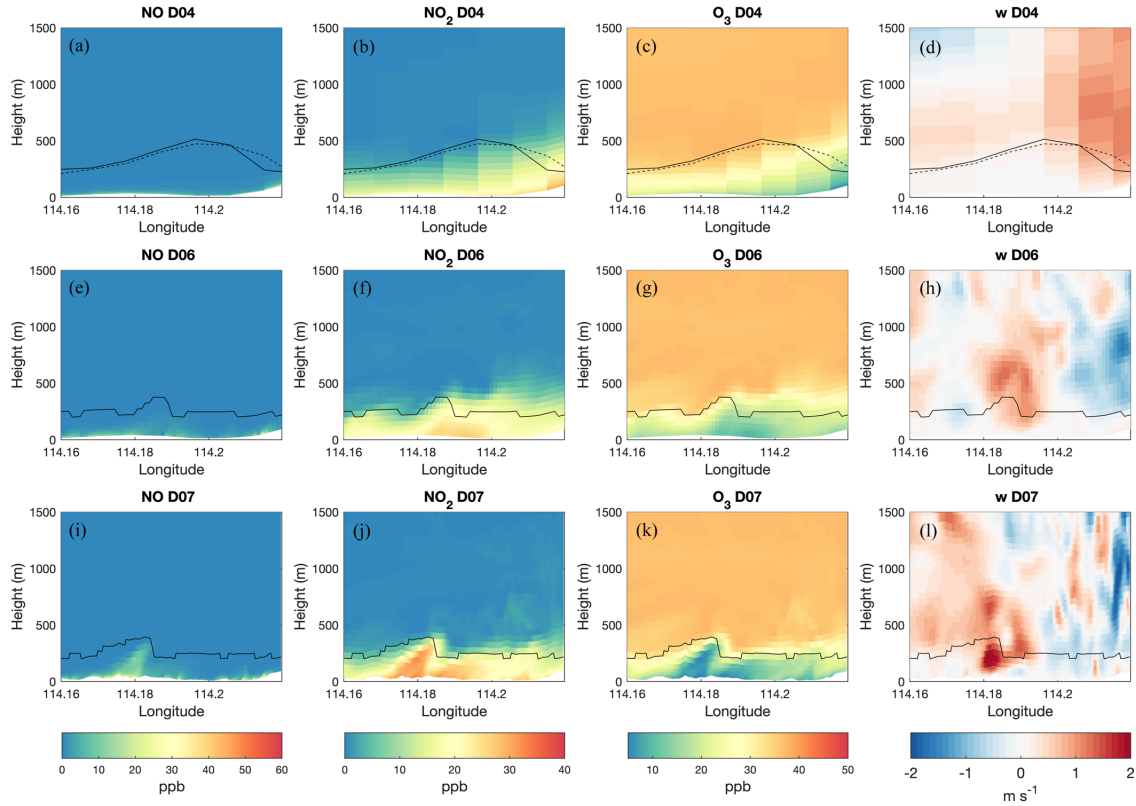
465
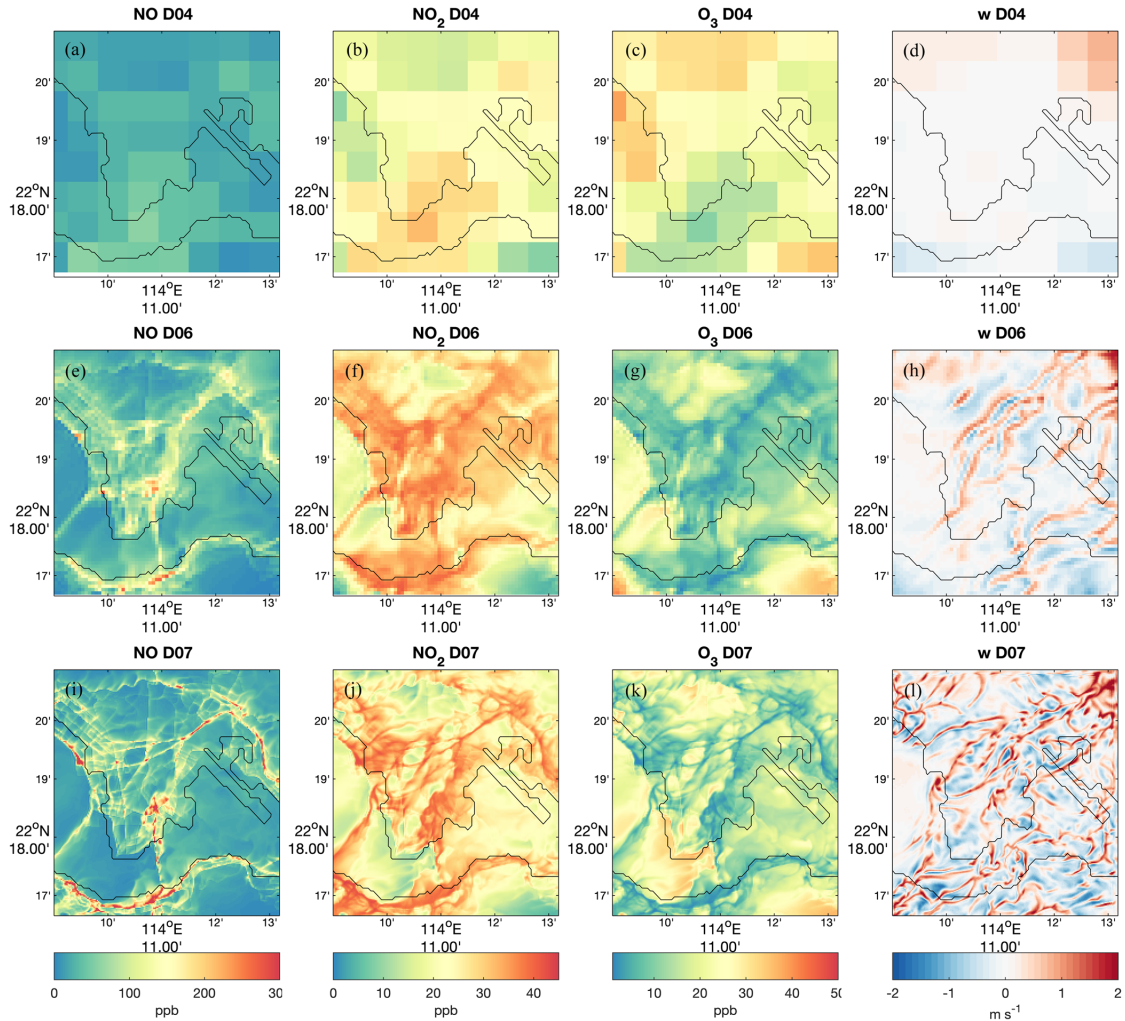
Figure 10. Horizontal distribution of simulated NO (first column), NO2 (second column), and O3 (third column) near surface at 13:00 LT for the D04 (first row), the D06 (second row), and the D07 (third row) cases. The fourth column provides the horizontal distribution of vertical wind (w) at approximately 100 m above ground.

470 The vertical distributions of the chemical species along the busy east-west Argyle Street (see Fig. 3b) in the vicinity of the Mong Kok station are shown in Fig. 11 (6:00 LT) and Fig. 12 (13:00 LT). In the early morning, the NO concentration is low, and the values are close to zero above the surface, implying weak surface emissions together with weak vertical mixing. The surface NO2 concentration becomes higher than that of NO, because of the higher O3 concentrations originating in the upper layers. The low O3 values at the surface are caused by the depletion of this molecule by NO. The vertical rate of mixing in the

475 mesoscale model is parameterized in the PBL, while it is directly calculated in the LES simulations. During the morning period, although the selected PBL scheme and the LES formulation produce similar PBL heights, the LES model produces a more detailed structure that better describes the vertical transport of the pollutants. At the noon time, the PBL height increases to about 1000 m due to the strong convective instability, which also can be seen from the sounding measurements in Fig. 5.

21

The surface NO concentrations are high along the road associated with the traffic emissions, and corresponding high NO$_2$ and
480   low O$_3$ concentration values. The vertical mixing of the chemical species at 13:00 LT is significantly stronger than in the
morning, because the PBL has become more convective. The vertical transport of the pollutants is higher in the mesoscale
simulation than the LESs, especially in the case of NO$_2$. This suggests that the YSU scheme produces strong vertical diffusion.
Compared with the coarse-resolution LES case (D06), the width of the high NO$_2$ and low O$_3$ concentration patterns within the
PBL in the high-resolution (D07) LES simulation is significantly reduced (about one to several hundred meters), and the width
485   of the low NO$_2$ and high O$_3$ patterns also decreases to the range of several hundred meters to one kilometer. This is related to
the thermal structure characterized by narrow updrafts and wide downdrafts during the well-developed phase of the turbulent
PBL (see Fig. 12l), which is subject to under-resolved convection effects widening these thermals at coarser grid spacings.

490   **Figure 11.** Vertical distribution of simulated NO (first column), NO$_2$ (second column), O$_3$ (third column) mixing ratios (ppbv), and vertical
wind velocity (w; fourth column) along a busy east-west road near the Mong Kok station (Argyle Street, see Fig. 3b) at 6:00 LT for the D04
(first row), D06 (second row), and D07 (third row) cases. The black solid lines represent the calculated PBLH, and the black dash line the
PBLH from the model output for the mesoscale domain, which is calculated in the YSU PBL scheme.
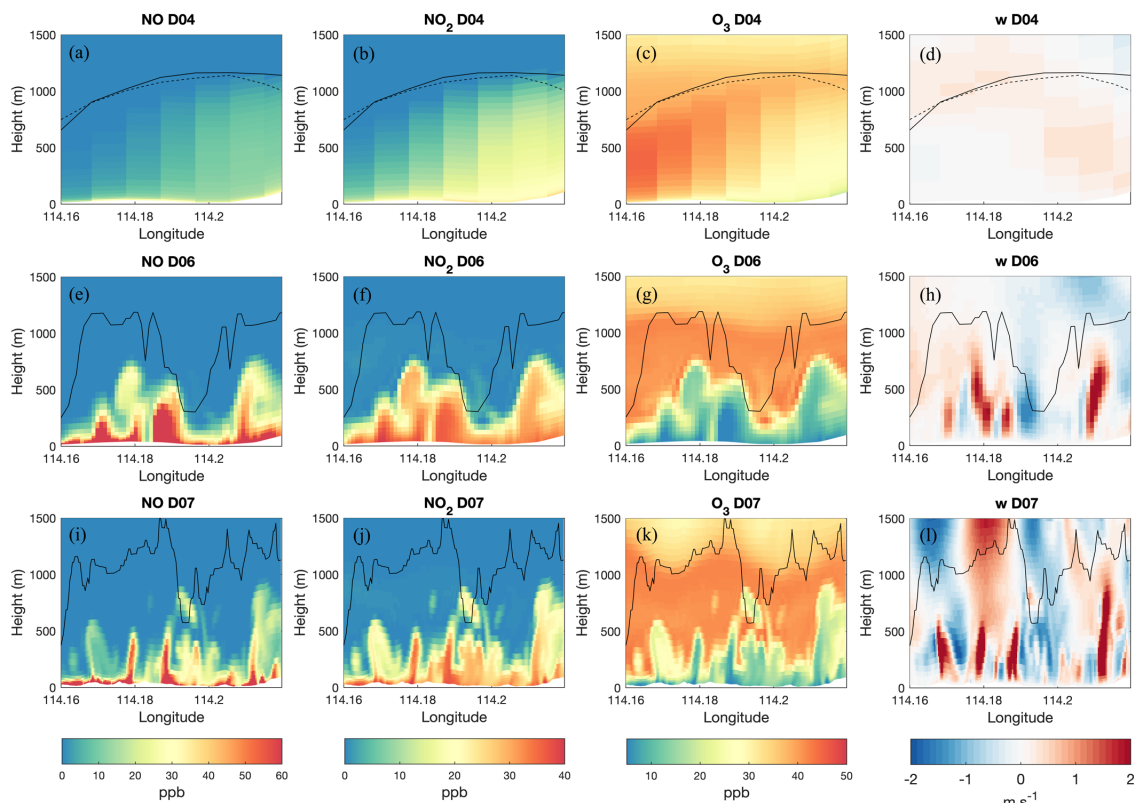
Figure 12. Vertical distribution of simulated NO (first column), NO_2 (second column), O_3 (third column) mixing ratios (ppbv), and vertical wind velocity (w; fourth column) along a busy east-west road near the Mong Kok station (Argyle Street, see Fig. 3b) at 13:00 LT for the D04 (first row), D06 (second row), and D07 (third row) cases. The black solid lines represent the calculated PBLH, and the black dash line the PBLH from the model output for the mesoscale domain, which is calculated in the YSU PBL scheme.

4.5 Development of vertical mixing of pollutants over a diurnal cycle

As shown in section 4.4, the vertical structure of the pollutants significantly varies with different model resolutions. To further evaluate the model behavior regarding the overall vertical mixing, the spatial and temporal averaged (over the subregion plotted in Fig. 9-10 and within one hour) profiles of the chemical species at different times of the day are shown in Fig. 13. To aid the interpretation of the vertical mixing with the boundary layer development, the diurnal variation of PBLH for selected domains is shown in Fig. 14. The PBLH is only about 200–300 m in the early morning when the boundary layer is still stable. As solar radiation intensifies, the PBLH starts to rise and reaches about 400–500 m at 8:00 LT. The PBLH continues to increase during the morning and reaches the highest altitude at noon time. The mean PBLH derived for the selected area D04 is 1088 m at 13:00 LT, which is similar to the height calculated for the sounding profile at the King's Park station. However, the mean PBLH is 768 m in the D06 LES simulation, which is considerably lower. This is possibly due to the local dynamics as seen in Fig. 12. The D07 LES is producing a PBLH (977 m) that is higher than the D06 LES simulation, but still 100 m lower than the mesoscale simulation. This indicates that the D06 LES underestimates the strength of the convective motions as it does not resolve turbulent eddies as accurately as the high-resolution LES (D07). In the afternoon, as the surface heat becomes weaker,

the PBLH decreases gradually. After sunset, the boundary layer becomes stable again, and the PBLHs decline rapidly to 393 m, 284 m, and 280 m respectively for the three domains.
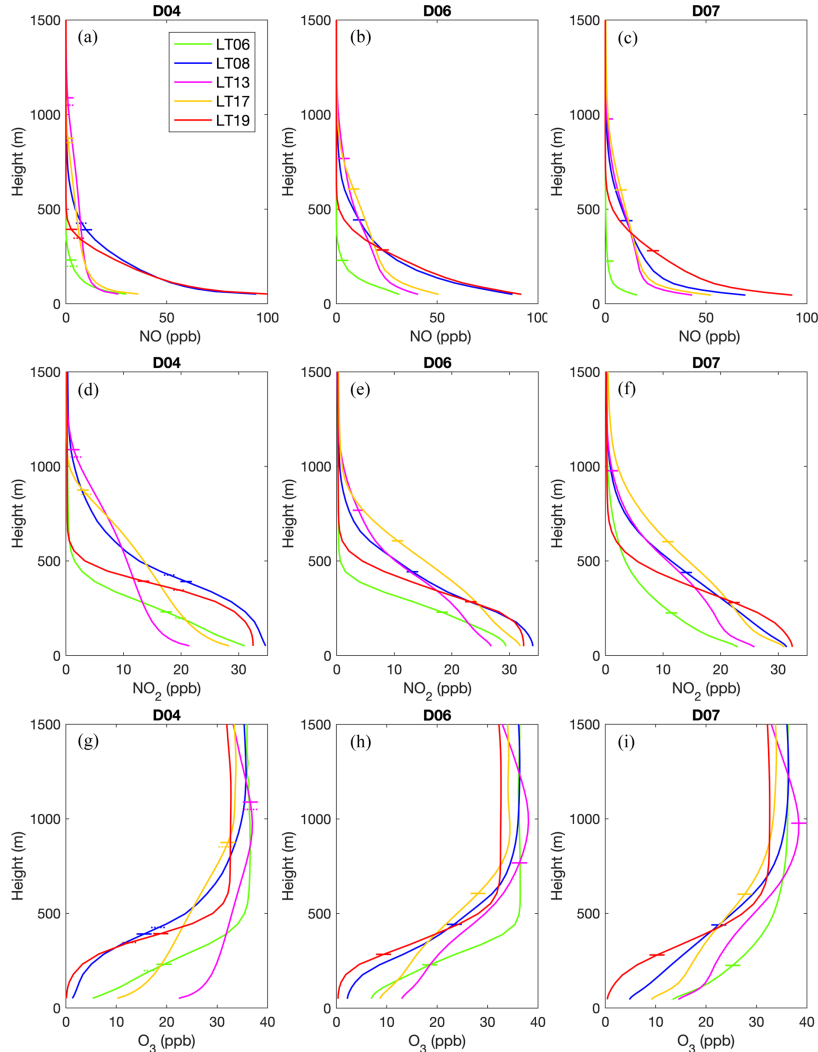
Figure 13. Horizontally averaged hourly mean profiles for the mixing ratio (ppbv) of chemical species (NO, NO_2 and O_3) over plotted region in Fig. 9–10 over the diurnal cycle on August 1, 2018. Different colors represent different times of the day: green – 6:00 LT, blue – 8:00 LT, magenta – 13:00 LT, yellow – 17:00 LT, red – 19:00 LT. Left column: simulation for D04 with resolution of 900 m; middle column: simulation for D06 with resolution of 100 m; right column: simulation from D07 with resolution of 33.3 m.

The simulated NO concentrations are highest near the surface and decrease rapidly against altitude. The mean NO concentrations are between 20 ppb and 30 ppb at the lowest layer of the model in the early morning and decline by a factor of 10 to 1 – 3 ppb at the PBLH. At about 200 m, the high-resolution LES (D07) provides lower NO concentrations relative to the low-resolution LES (D06) and the mesoscale simulation (D04). In other words, the vertical transport of NO is weakest in D07 in the early morning. As the strength of traffic pollution increases during the morning rush hour, the surface NO concentrations increase rapidly to 70 – 90 ppb in the three simulations and reach values that are about three times higher than those at 6:00

24

525   LT. The coarse resolution model produces surface NO values that are larger than in the high-resolution LESs; however, the NO concentrations at the PBLH are about 10 ppb in all three simulations with higher PBLH derived in the LES simulations. This implies the faster development of the boundary layer and the stronger vertical mixing in the high-resolution LES. The surface concentration of NO decreases around noon due to the reduction of the road emissions after the rush hour. In contrast with the morning profiles, the D07 LES simulation exhibits high surface NO concentrations. Indeed, values derived in the D07

530   case are about twice as high as the values produced by the mesoscale simulations. However, the vertical mixing of NO above 500 m is stronger in the mesoscale simulation in which the PBL is parameterized. This is related to the higher PBLH produced in the D04 simulation for the convective dominated noon condition. The strong vertical transport extends into the afternoon, and the profiles at 17:00 LT are similar to those at 13:00 LT. The NO concentrations above 500 m start to decrease in the evening as the PBL height decreases; however, the surface NO concentration rises again during the evening rush hour at 19:00.

535   It also shows in the high-resolution LES simulations significantly higher NO concentrations in the residual layer.
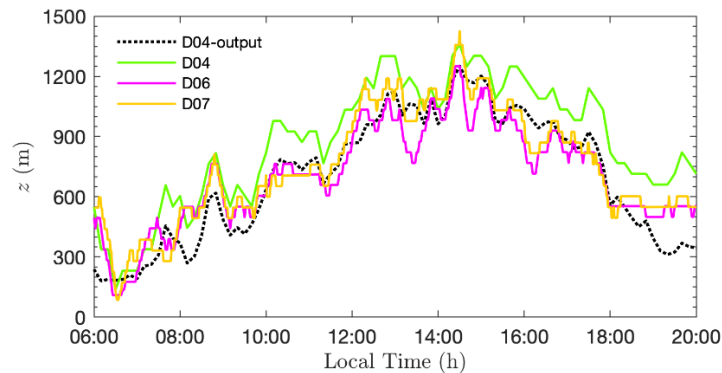

Figure 14. Horizontally averaged PBLH over plotted region in Fig. 9–10 over the diurnal cycle on August 1, 2018. Different colors of the solid lines represent different model resolutions: green – D04 (900 m), magenta – D06 (100 m), yellow – D07 (33.3 m).

       The patterns that characterize the NO_2 mean profiles are different from those of NO. The peak values of NO_2 are also located

540   at the surface, due to the large amount of NO, but the decay rate against altitude is slower than that of NO. At 6:00 LT, the surface NO_2 concentrations are about 30 ppb in the D04 and D06 simulations and approximately 25 ppb in the D07 LES case. The corresponding concentrations at PBLH are 17 ppb, 18 ppb, and 12 ppb for the three simulations, equivalent to approximately 50% of the surface level concentrations. Compared to the other two simulations, the D07 LES exhibits higher NO_2 concentrations above the PBLH, implying strong conversion of NO to NO_2. With the increase of traffic emissions in the

545   morning rush hour at 8:00 LT, the NO_2 concentrations did not rise as much as NO, possibly due to the onset of the photolysis. In the morning, the NO_2 concentrations in the upper boundary further increase with the development of the convection in the PBL. Similar to the situation with NO, the mesoscale model generates stronger vertical mixing of NO_2 at noon compared to the LES simulations. The situation is opposite in the afternoon: the NO_2 concentrations near the PBLH at 17:00 LT became lower than the noon time in the mesoscale simulation, while they continue to increase in the D07 LES. This reveals that the

550   decay of convective condition occurs later in the LES than in the mesoscale model. During the evening hours, the air masses

with high NO$_2$ values move down with the height of the PBL, and, at the same time, the surface NO$_2$ concentrations increase due to the continuous surface emissions and the reduction in the photolysis rates.

The O$_3$ concentration profiles generally exhibit opposite patterns relative to NO$_2$, in response to the titration by NO. The O$_3$ concentrations above the boundary layer are mostly influenced by the background levels, which are between 30 ppb and 40 ppb. In the early morning the surface O$_3$ concentration is about 5 ppb in the D04 case, 7 ppb in the D06 case, and 12 ppb in the D07 case, respectively; these values are related to the NO concentrations in the different simulations. The surface O$_3$ is reduced at 8:00 LT by the depletion of NO that is released by traffic emissions during the rush hour. The O$_3$ levels in the mixed layer are replenished through subsidence from the upper layers during the day, which results in the rise of O$_3$ during the afternoon. In the evening, O$_3$ concentrations decrease again because of the slower downward transport and the titration by the NO emitted from traffic roads.
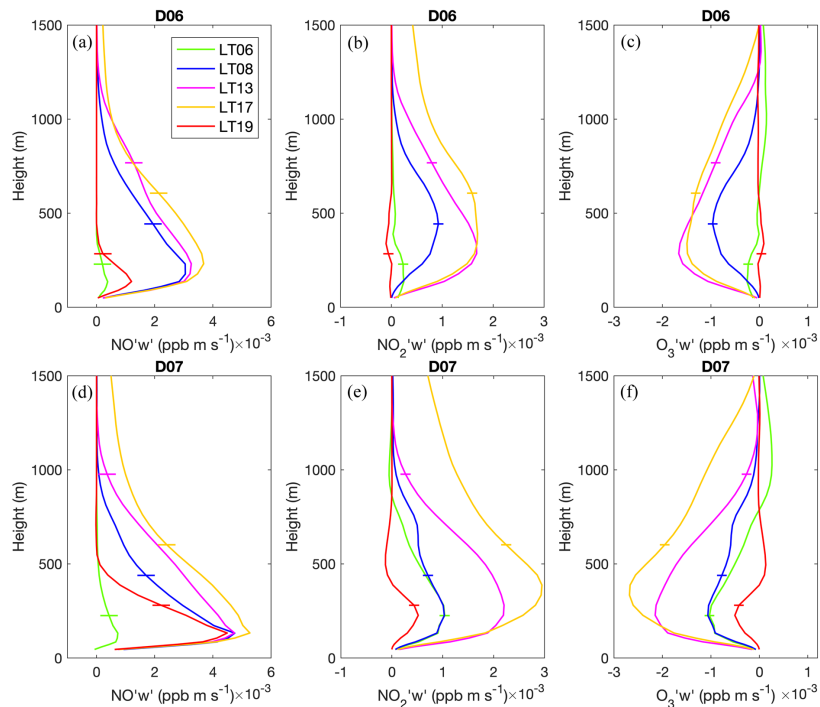
Figure 15. Horizontally averaged hourly mean profiles of the vertical fluxes of NO (left), NO$_2$ (middle), and O$_3$ (right) in selected regions highlighting the diurnal cycle on August 1, 2018.

The vertical fluxes of the chemical species are calculated for the LES simulations with different horizontal resolutions. The horizontally averaged flux profiles over the selected region at different times are shown in Fig. 15. For NO, the vertical fluxes are positive, indicating net upward transport during the entire diurnal cycle. The peak of the NO fluxes appears to be located between the heights of 100 m and 200 m, in a layer where the turbulent motion is strong. The vertical fluxes of NO are smallest at 6:00 LT, when the boundary is stable, and then increases substantially with the development of the PBL after sunrise and the increase in traffic emissions around 8:00 LT. This enhancement of the NO fluxes continues into the afternoon as the convection in the PBL keeps growing, and the peaks of the flux profiles are gradually lifted up. The upward transport becomes

26

weaker again in the evening when the boundary layer becomes stable. For NO_2, the vertical fluxes are also essentially positive, except right above the PBL in the evening. The peaks in the NO_2 upward fluxes are higher than those in NO, because of the smaller gradient in the concentration profiles (Fig. 13). The NO_2 fluxes above the PBLH are larger than the fluxes of NO, because of the atmospheric photochemical production of NO_2. For O_3, the vertical fluxes are generally negative, indicating the downward transport from the upper atmospheric layers, and the pattern of the O_3 fluxes is opposite to that of NO_2. As expected, the 33.3-m LES produces larger resolved vertical fluxes than the 100-m LES, while the patterns are similar for the two cases. This indicates that the high-resolution LES better represents the turbulent motions, and generates stronger vertical mixing in the convective boundary layer. This is consistent with the analysis of concentration profiles.

5 Conclusions

In this paper, we present high-resolution air quality simulations using the WRF model coupled with an LES module and with an interactive (online) chemical mechanism. This directly coupled mesoscale-to-LES model within the WRF frame ensures the consistency between the physical and chemical processes among scales. In addition to the regular emission inventories used by the coarse models, line sources of the traffic emissions are incorporated to the high LES resolutions. The performance of the WRF-LES-Chem model is evaluated in the megacity of Hong Kong, which is exposed to multi-type chemical sources and to complex topography. The multi-resolution simulations from mesoscale to LES scale are evaluated by comparing the calculated concentrations to ozone sounding profiles and measurements from the surface monitoring network. The spatial distributions of the chemical species represented by simulations with different resolutions are analyzed to demonstrate the capability of the model to reproduce the transformation of the pollutants in turbulent flows. The patterns of the vertical mixing of the chemical species are also presented to evaluate the model behavior during the diurnal evolution of the boundary layer.

The comparison with the ozone sounding measurements indicates that the coarser resolution model fails to reproduce the vertical structure of O_3 concentrations, while the higher resolution LES improves the performance near the surface with a better representation of the local emissions. However, large discrepancies still exist in the middle of the boundary layer, which is possibly due to the biases in the wind prediction.

The simulated NO_X and O_3 concentrations were validated relative to the Hong Kong EPD surface observations at 16 stations, including 3 roadside stations and 13 general stations. Both mesoscale and LES simulations successfully reproduce the mean concentrations and the diurnal variations at the general stations, especially at the stations in the suburban areas of the city. The improvement provided by the LES formulation is limited when considering the background concentrations of the pollutants. At the roadside stations, the mesoscale simulation largely underestimates the NO_X concentrations and overestimates O_3 due to the coarse representation of the traffic emissions. The LES simulations improve the agreements with the measurements, especially the simulation performed with a 33.3-m grid spacing. However, a statistical analysis of the results shows that an increase in the LES resolution from 100 m to 33.3 m does not always improve the model results relative to local measurements.

The LES simulations provide more detailed structures of the spatial distributions of the chemical species relative to the mesoscale simulations, because the LES formulation resolves the large turbulent eddies. This is more clearly illustrated when the PBL is well developed at noon time. The 33.3-m LES provides more vigorous turbulence than the 100-m LES, and thus stronger vertical mixing of the pollutants. The mean profiles of the chemical species at different times are controlled by the diurnal cycle of the surface emissions, the photolysis rate, and the development of the boundary layer. The simulations with different resolutions show similar trends in the diurnal evolution of the profiles of the chemical species in the boundary layer with some offset time.

The evaluation of the coupled WRF-LES-Chem model shows that the LES simulations provide more detailed distributions of the pollutants resulting from the more detailed representation of the emissions and the explicit representation of the most energy-carrying turbulence structures. The LES simulations should be further improved with the adoption of real-time traffic emissions rather than the yearly-averaged values used in this work. The multi-scale LES simulation provides encouraging results for future accurate forecasts of air quality in large cities with heavy pollution. Such approach has great potential for operational forecasting in the future with the availability of increasing of the computing resources that enable representation of resolved building effects at grid spacings smaller than 10 m. Some optimizations should be introduced in the next model developments. Since the WRF system is based on a terrain-following coordinate, which makes resolving buildings difficult, some alternative meshing techniques (e.g., the immersed boundary method, IBM, Lundquist et al., 2010; 2012) might have to be considered. Some work has been performed to accelerate the WRF system by leveraging GPUs. With such further developments of the model system, opportunities exist for optimizing the WRF-LES-Chem in future operational air quality forecasting.

Code and data availability. The WRF model is public available at https://www2.mmm.ucar.edu/wrf/users/. The air quality data at surface stations are public available on the Hong Kong EPD's website: https://cd.epic.epd.gov.hk/EPICDI/air/station/?lang=en. The ozone sounding data are downloaded from the World Ozone and Ultraviolet Radiation Data Centre: https://woudc.org/home.php.

Author contributions. Conceptualization, GPB and YW; methodology, YW and YFM; software, YW, YFM, DME, and JD; validation, YW; formal analysis, YW; investigation, YW; resources, RCWT; data curation, YW; visualization, YW and YFM; writing—original draft preparation, YW and YFM; writing—review and editing, GPB, CWYL, PL, DME, and CHL; supervision, GPB and TW; project administration, TW; funding acquisition, TW. All authors have read and agreed to the published version of the manuscript.

Competing interests. The authors declare that they have no conflict of interest.

References

Baik, J.-J., Park, S.-B., and Kim, J.-J.: Urban flow and dispersion simulation using a CFD model coupled to a mesoscale model, J. Appl. Meteorol. Climatol., 48(8), 1667–1681, https://doi.org/10.1175/2009JAMC2066.1, 2009.

Barzyk, T. M., Isakov, V., Arunachalam, S., Venkatram, A., Cook, R., and Naess, B.: A near-road modeling system for
640 community-scale assessments of traffic-related air pollution in the United States, Environ. Model. Softw 66, 46–56, https://doi.org/10.1016/j.envsoft.2014.12.004, 2015.

Batterman, S., Chambliss, S., and Isakov, V.: Spatial resolution requirements for traffic-related air pollutant exposure evaluations. Atmos. Environ., 94, 518–528, https://doi.org/10.1016/j.atmosenv.2014.05.065, 2014.

Beare, R. J.: The role of shear in the morning transition boundary layer, Bound.-Layer Meteorol., 129(3), 395–410,
645 https://doi.org/10.1007/s10546-008-9324-8, 2008.

Bian, Y., Huang, Z., Ou, J., Zhong, Z., Xu, Y., Zhang, Z., Xiao, X., Ye, X., Wu, Y., Yin, X., Li, C., Chen, L., Shao, M., and Zheng, J.: Evolution of anthropogenic air pollutant emissions in Guangdong Province, China, from 2006 to 2015, Atmos. Chem. Phys., 19(18), 11701–11719, https://doi.org/10.5194/acp-19-11701-2019, 2019.

Buchholz, R. R., Emmons, L. K., Tilmes, S., and Team, T. C. D.: CESM2.1/CAM-chem Instantaneous Output for Boundary
650 Conditions, UCAR/NCAR [data set]. Subset used Lat: 0 to 50, Lon: 80 to 140, 30 Jul - 1Aug 2018, Accessed 8 Aug 2021. https://doi.org/10.5065/NMP7-EP60, 2019.

Chen, F., & Dudhia, J.: Coupling an advanced land surface-hydrology model with the Penn State-NCAR MM5 modeling system. Part I: Model implementation and sensitivity, Mon. Weather Rev., 129(4), 569–585, https://doi.org/10.1175/1520-0493(2001)129<0569:CAALSH>2.0.CO;2, 2001.

655 Chou, M. D. S., M.J.: An efficient thermal infrared radiation parameterization for use in general circulations models, in: Volume 3 technical report series on global modeling and data assimilation, Greenbelt, MD: NASA Goddard Space Flight Center, Tech. Mem. 104606, 85 pp., 1994.

Deardorff, J. W.: A numerical study of three-dimensional turbulent channel flow at large Reynolds numbers, J. Fluid Mech., 41(2), 453–480, https://doi.org/10.1017/S0022112070000691, 1970.

660 Emmons, L. K., Schwantes, R. H., Orlando, J. J., Tyndall, G., Kinnison, D., Lamarque, J. F., Marsh, D., Mills, M. J., Tilmes, S., Bardeen, C., Buchholz, R. R., Conley, A., Gettelman, A., Garcia, R., Simpson, I., Blake, D. R., Meinardi, S., and Pétron, G.: The chemistry mechanism in the Community Earth System Model Version 2 (CESM2), J. Adv. Model. Earth Syst., 12(4), e2019MS001882, https://doi.org/10.1029/2019MS001882, 2020.

Forehead, H., and Huynh, N.: Review of modelling air pollution from traffic at street-level - The state of the science, Environ.
665 Pollut., 241, 775–786, https://doi.org/10.1016/j.envpol.2018.06.019, 2018.

Friedl, M. A., Strahler, A. H., Hodges, J., Hall, F. G., Collatz, G. J., Meeson, B. W., Los, S. O., De Colstoun, E. B., and Landis, D. R.: ISLSCP II MODIS (Collection 4) IGBP Land Cover, 2000-2001, ORNL DAAC [data set]. https://doi.org/10.3334/ORNLDAAC/968, 2010.

Garratt, J. R.: Review: the atmospheric boundary layer, Earth-Sci. Rev., 37(1), 89–134, https://doi.org/10.1016/0012-8252(94)90026-4, 1994.

Gaudet, B. J., Lauvaux, T., Deng, A., and Davis, K. J.: Exploration of the impact of nearby sources on urban atmospheric inversions using large eddy simulation, Elementa: Sci. Anthro., 5(60), 1–22, https://doi.org/10.1525/elementa.247, 2017.

Grell, G. A., and Freitas, S. R.: A scale and aerosol aware stochastic convective parameterization for weather and air quality modeling, Atmos. Chem. Phys., 14(10), 5233–5250, https://doi.org/10.5194/acp-14-5233-2014, 2014.

Grell, G. A., Peckham, S. E., Schmitz, R., McKeen, S. A., Frost, G., Skamarock, W. C., and Eder, B.: Fully coupled "online" chemistry within the WRF model, Atmos. Environ., 39(37), 6957–6975, https://doi.org/10.1016/j.atmosenv.2005.04.027, 2005.

Guenther, A., Karl, T., Harley, P., Wiedinmyer, C., Palmer, P. I., and Geron, C.: Estimates of global terrestrial isoprene emissions using MEGAN (Model of Emissions of Gases and Aerosols from Nature), Atmos. Chem. Phys., 6(11), 3181–3210, https://doi.org/10.5194/acp-6-3181-2006, 2006.

Hong, S.-Y., Noh, Y., and Dudhia, J.: A new vertical diffusion package with an explicit treatment of entrainment processes, Mon. Weather Rev., 134(9), 2318–2341, https://doi.org/10.1175/MWR3199.1, 2006.

Jiménez, P. A., Dudhia, J., González-Rouco, J. F., Navarro, J., Montávez, J. P., and García-Bustamante, E.: A revised scheme for the WRF wurface layer formulation. Mon. Weather Rev., 140(3), 898–918, https://doi.org/10.1175/MWR-D-11-00056.1, 2012.

Johansson, L., Jalkanen, J.-P., and Kukkonen, J.: Global assessment of shipping emissions in 2015 on a high spatial and temporal resolution, Atmos. Environ., 167, 403–415, https://doi.org/10.1016/j.atmosenv.2017.08.042, 2017.

Khan, B., Banzhaf, S., Chan, E. C., Forkel, R., Kanani-Sühring, F., Ketelsen, K., Kurppa, M., Maronga, B., Mauder, M., Raasch, S., Russo, E., Schaap, M., and Sühring, M.: Development of an atmospheric chemistry model coupled to the PALM model system 6.0: implementation and first applications, Geosci. Model Dev., 14(2), 1171–1193, https://doi.org/10.5194/gmd-14-1171-2021, 2021.

Li, C. W. Y., Brasseur, G. P., Schmidt, H., and Mellado, J. P.: Error induced by neglecting subgrid chemical segregation due to inefficient turbulent mixing in regional chemical-transport models in urban environments, Atmos. Chem. Phys., 21(1), 483–503, https://doi.org/10.5194/acp-21-483-2021, 2021.

Li, M., Zhang, Q., Kurokawa, J.-I., Woo, J.-H., He, K., Lu, Z., Ohara, T., Song, Y., Streets, D. G., Carmichael, G. R., Cheng, Y., Hong, C., Huo, H., Jiang, X., Kang, S., Liu, F., Su, H., and Zheng, B.: MIX: a mosaic Asian anthropogenic emission inventory under the international collaboration framework of the MICS-Asia and HTAP, Atmos. Chem. Phys., 17(2), 935–963. https://doi.org/10.5194/acp-17-935-2017, 2017.

Lin, Y.-L., Farley, R. D., and Orville, H. D.: Bulk parameterization of the snow field in a cloud model, J. Appl. Meteorol. Climatol., 22(6), 1065–1092, https://doi.org/10.1175/1520-0450(1983)022<1065:BPOTSF>2.0.CO;2, 1983.

Lin, D., Khan, B., Katurji, M., Bird, L., Faria, R., and Revell, L. E.: WRF4PALM v1.0: a mesoscale dynamical driver for the microscale PALM model system 6.0, Geosci. Model Dev., 14, 2503-2524, 10.5194/gmd-14-2503-2021, 2021.

Lundquist, K. A., Chow, F. K., and LUNDQUIST, J. K.: An Immersed Boundary Method for the Weather Research and Forecasting Model, Monthly Weather Review, 138, 796-817, 10.1175/2009mwr2990.1, 2010.

Lundquist, K. A., Chow, F. K., and Lundquist, J. K.: An Immersed Boundary Method Enabling Large-Eddy Simulations of Flow over Complex Terrain in the WRF Model, Monthly Weather Review, 140, 3936-3955, https://doi.org/10.1175/MWR-D-11-00311.1, 2012.

Maronga, B., Banzhaf, S., Burmeister, C., Esch, T., Forkel, R., Fröhlich, D., Fuka, V., Gehrke, K. F., Geletič, J., Giersch, S., Gronemeier, T., Groß, G., Heldens, W., Hellsten, A., Hoffmann, F., Inagaki, A., Kadasch, E., Kanani-Sühring, F., Ketelsen, K., Khan, B. A., Knigge, C., Knoop, H., Krč, P., Kurppa, M., Maamari, H., Matzarakis, A., Mauder, M., Pallasch, M., Pavlik, D., Pfafferott, J., Resler, J., Rissmann, S., Russo, E., Salim, M., Schrempf, M., Schwenkel, J., Seckmeyer, G., Schubert, S.,

Sühring, M., von Tils, R., Vollmer, L., Ward, S., Witha, B., Wurps, H., Zeidler, J., and Raasch, S.: Overview of the PALM model system 6.0, Geosci. Model Dev., 13(3), 1335–1372, https://doi.org/10.5194/gmd-13-1335-2020, 2020.

715 Maronga, B., Gross, G., Raasch, S., Banzhaf, S., Forkel, R., Heldens, W., Kanani-Sühring, F., Matzarakis, A., Mauder, M., Pavlik, D., Pfafferott, J., Schubert, S., Seckmeyer, G., Sieker, H., and Winderlich, K.: Development of a new urban climate model based on the model PALM – Project overview, planned work, and first achievements. Meteorol. Zeitschrift, 28(2), 105–119, https://doi.org/10.1127/metz/2019/0909, 2019.

Mlawer, E. J., Taubman, S. J., Brown, P. D., Iacono, M. J., and Clough, S. A.: Radiative transfer for inhomogeneous atmospheres: RRTM, a validated correlated-k model for the longwave, J. Geophys. Res. Atmos., 102(D14), 16663–16682, 720 https://doi.org/10.1029/97JD00237, 1997.

Moeng, C.-H.: A large-eddy-simulation model for the study of planetary boundary-layer turbulence, J. Atmos. Sci., 41(13), 2052–2062, https://doi.org/10.1175/1520-0469(1984)041<2052:ALESMF>2.0.CO;2, 1984.

Moeng, C. H., Dudhia, J., Klemp, J., and Sullivan, P.: Examining Two-Way Grid Nesting for Large Eddy Simulation of the PBL Using the WRF Model, Mon. Weather Rev., 135(6), 2295-2311, https://doi.org/10.1175/mwr3406.1, 2007.

725 Muñoz-Esparza, D., Kosović, B., Mirocha, J., and van Beeck, J.: Bridging the transition from mesoscale to microscale turbulence in numerical weather prediction models, Bound.-Layer Meteorol., 153(3), 409–440, https://doi.org/10.1007/s10546-014-9956-9, 2014.

Muñoz-Esparza, D., Kosović, B., van Beeck, J., and Mirocha, J.: A stochastic perturbation method to generate inflow turbulence in large-eddy simulation models: Application to neutrally stratified atmospheric boundary layers, Phys. Fluids, 730 27(3), 035102, https://doi.org/10.1063/1.4913572, 2015.

Muñoz-Esparza, D., Lundquist, J. K., Sauer, J. A., Kosović, B., and Linn, R. R.: Coupled mesoscale-LES modeling of a diurnal cycle during the CWEX-13 field campaign: From weather to boundary-layer eddies, J. Adv. Model. Earth Syst., 9(3), 1572–1594, https://doi.org/10.1002/2017MS000960, 2017.

Muñoz-Esparza, D. and Kosović, B.: Generation of Inflow Turbulence in Large-Eddy Simulations of Nonneutral Atmospheric 735 Boundary Layers with the Cell Perturbation Method, Monthly Weather Review, 146, 1889-1909, 10.1175/mwr-d-18-0077.1, 2018.

Muñoz-Esparza, D., Sauer, J. A., Shin, H. H., Sharman, R., Kosović, B., Meech, S., García-Sánchez, C., Steiner, M., Knievel, J., Pinto, J., and Swerdlin, S.: Inclusion of building-resolving capabilities into the FastEddy® GPU-LES model using an immersed body force method, J. Adv. Model. Earth Syst., 12(11), e2020MS002141, https://doi.org/10.1029/2020MS002141, 740 2020.

Muñoz-Esparza, D., Shin, H. H., Sauer, J. A., Steiner, M., Hawbecker, P., Boehnert, J., Pinto, J. O., Kosović, B., and Sharman, R. D.: Efficient graphics processing unit modeling of street-scale weather effects in support of aerial operations in the urban environment, AGU Adv., 2(2), e2021AV000432, https://doi.org/10.1029/2021AV000432, 2021.

Nottrott, A., Kleissl, J., and Keeling, R.: Modeling passive scalar dispersion in the atmospheric boundary layer with WRF 745 large-eddy simulation, Atmos. Environ., 82, 172–182, https://doi.org/10.1016/j.atmosenv.2013.10.026, 2017.

Nozawa, K., and Tamura, T.: Coupling method of WRF-LES and LES based on scale similarity model, in: Proceedings of the 7th International Colloquium on Bluff Body Aerodynamics and Applications (BBAA7), Shanghai, China, 2-6 September 2012, 1942–1949, 2012.

Sauer, J. A., and Muñoz-Esparza, D.: The FastEddy® resident-GPU accelerated large-eddy simulation framework: Model 750 formulation, dynamical-core validation and performance benchmarks, J. Adv. Model. Earth Syst., 12(11), e2020MS002100, https://doi.org/10.1029/2020MS002100, 2020.

Skamarock, W. C., Klemp, J.B., Dudhia, J., Gill, D.O., Liu, Z., Berner, J., Wang, W., Powers, J.G., Duda, M.G., Barker, D.M., and Huang, X.-Y.: A description of the advanced research WRF model version 4.1, Boulder, CO: National Center for Atmospheric Research, Tech. Rep. NCAR/TN-556+STR, 145 pp., https://doi.org/10.5065/1dfh-6p97, 2019.

755 Smagorinsky, J.: General circulation experiments with the primitive equations: I. The basic experiment, Mon. Weather Rev., 91(3), 99–164, https://doi.org/10.1175/1520-0493(1963)091<0099:GCEWTP>2.3.CO;2, 1963.

Stockwell, W. R., Middleton, P., Chang, J. S., and Tang, X.: The second generation regional acid deposition model chemical mechanism for regional air quality modeling, J. Geophys. Res. Atmos., 95(D10), 16343–16367, https://doi.org/10.1029/JD095iD10p16343, 1990.

760 Takaku, J., Tadono, T., and Tsutsui, K.: Generation of high resolution global DSM from ALOS PRISM, The International Archives of the Photogrammetry, Remote Sensing and Spatial Information Sciences, XL-4, 243–248, https://doi.org/10.5194/isprsarchives-XL-4-243-2014, 2014.

Tominaga, Y., and Stathopoulos, T.: CFD simulation of near-field pollutant dispersion in the urban environment: A review of current modeling techniques, Atmos. Environ., 79, 716–730, https://doi.org/10.1016/j.atmosenv.2013.07.028, 2013.

765 Wang, T., Xue, L., Brimblecombe, P., Lam, Y. F., Li, L., and Zhang, L.: Ozone pollution in China: A review of concentrations, meteorological influences, chemical precursors, and effects, Sci. Total Environ., 575, 1582–1596, https://doi.org/10.1016/j.scitotenv.2016.10.081, 2017.

Wang, Y., Brasseur, G. P., and Wang, T.: Segregation of atmospheric oxidants in turbulent urban environments, Atmosphere, 13(2), 315, https://doi.org/10.3390/atmos13020315, 2022.

770 Wang, Y., Ma, Y.-F., Muñoz-Esparza, D., Li, C. W. Y., Barth, M., Wang, T., and Brasseur, G. P. (2021). The impact of inhomogeneous emissions and topography on ozone photochemistry in the vicinity of Hong Kong Island, Atmos. Chem. Phys., 21(5), 3531–3553, https://doi.org/10.5194/acp-21-3531-2021, 2021.

WHO: Review of evidence on health aspects of air pollution – REVIHAAP project, Copenhagen: WHO Regional Office for Europe, Tech. Rep. 27195369, https://www.ncbi.nlm.nih.gov/books/NBK361805, 2013.

775 Yamaguchi, T., and Feingold, G.: Technical note: Large-eddy simulation of cloudy boundary layer with the Advanced Research WRF model, J. Adv. Model. Earth Syst., 4, M09003, https://doi.org/10.1029/2012MS000164, 2012.

Zheng, B., Tong, D., Li, M., Liu, F., Hong, C., Geng, G., Li, H., Li, X., Peng, L., Qi, J., Yan, L., Zhang, Y., Zhao, H., Zheng, Y., He, K., and Zhang, Q.: Trends in China's anthropogenic emissions since 2010 as the consequence of clean air actions, Atmos. Chem. Phys., 18(19), 14095–14111, https://doi.org/10.5194/acp-18-14095-2018, 2018.

780 Zheng, J., Zhang, L., Che, W., Zheng, Z., and Yin, S.: A highly resolved temporal and spatial air pollutant emission inventory for the Pearl River Delta region, China and its uncertainty assessment, Atmos. Environ., 43(32), 5112–5122, https://doi.org/10.1016/j.atmosenv.2009.04.060, 2009.

Zheng, Y., Miao, Y., Liu, S., Chen, B., Zheng, H., & Wang, S.: Simulating flow and dispersion by using WRF-CFD coupled model in a built-up area of Shenyang, China. Adv. Meteorol., 2015, 528618, https://doi.org/10.1155/2015/528618, 2015.

785 Zhong, J., Cai, X.-M., and Bloss, W. J.: Coupling dynamics and chemistry in the air pollution modelling of street canyons: A review, Environ. Pollut., 214, 690–704, https://doi.org/10.1016/j.envpol.2016.04.052, 2016.